

GRAND3 — Ground structure based topology optimization for arbitrary 3D domains using MATLAB

Tomás Zegard¹ · Glaucio H. Paulino¹

Received: 4 November 2014 / Revised: 11 April 2015 / Accepted: 7 June 2015 / Published online: 23 July 2015
© Springer-Verlag Berlin Heidelberg 2015

Abstract Since its introduction, the ground structure method has been used in the derivation of closed-form analytical solutions for optimal structures, as well as providing information on the optimal load-paths. Despite its long history, the method has seen little use in three-dimensional problems or in problems with non-orthogonal domains, mainly due to computational implementation difficulties. This work presents a methodology for ground structure based topology optimization in arbitrary three-dimensional (3D) domains. The proposed approach is able to address concave domains and with the possibility of holes. In addition, an easy-to-use implementation of the proposed algorithm for the optimization of least-weight trusses is described in detail. The method is verified against three-dimensional closed-form solutions available in the literature. By means of examples, various features of the 3D ground structure approach are assessed, including the ability of the method to provide solutions with different levels of detail. The source code for a MATLAB implementation of the method, named GRAND3 — *G*round *s*tructure *A*nalysis and *D*esign in 3D, is available in the (electronic) *Supplementary Material* accompanying this publication.

Keywords Ground structure method · Topology optimization of three-dimensional trusses · Three-dimensional optimal structures · Unstructured meshes · Intersection tests

1 Introduction

The ground structure method (Dorn et al. 1964), is a discrete element topology optimization approach that can address relatively large problems on standard computers. Using a reduced (finite) number of discrete elements, the method can provide an approximation to the optimal Michell structure (Michell 1904; Hemp 1973), composed of an infinite number of members. The limited computational capability and lack of flexibility in current methods are to blame for the decreased interest in three-dimensional topology optimization. The problem of finding the least-weight (least volume) truss for a single load case, under elastic and linear conditions, subjected to stress constraints can be posed as a linear programming problem (Ohsaki 2010), and is the base of the method's efficiency. The ground structure method tackles the topology optimization problem (sizing and geometry), as a sizing-only optimization problem for a highly interconnected and redundant truss, i.e. the *ground structure*.

The authors' previous work (Zegard and Paulino 2014) in 2D, generates the ground structure using linear algebra operations. Members generated in concave regions or holes are detected and removed using collision tests, in an approach derived from the video-game and ray-tracing literature. In the present work, it will be shown that this approach can successfully scale to three-dimensional space, provided that the 3D analogues to the two-dimensional collision tests are developed. The algorithms are described in detail, and a MATLAB implementation of the method is provided, which is also used to provide examples and show the capabilities

Electronic supplementary material The online version of this article (doi:10.1007/s00158-015-1284-2) contains supplementary material, which is available to authorized users.

✉ Glaucio H. Paulino
paulino@illinois.edu

¹ Department of Civil and Environmental Engineering,
Newmark Laboratory, University of Illinois
at Urbana–Champaign, 205 N. Mathews
Avenue, Urbana, IL 61801, USA

and limitations of the proposed method. Before addressing problems for which the solution is not known, the proposed method is verified against known solutions available in the literature.

Three-dimensional ground structure analysis has been successfully performed in the past (Gerdes 1994; Smith 1998; Gilbert et al. 2005; Tyas et al. 2006). Unfortunately, most of these works are restricted to structured and orthogonal discretizations. The interest in unstructured non-orthogonal domains is reasonable considering that applied engineering problems are often not *boxes* and may include geometrical constraints such as holes. The method does require the domain to be discretized, and as a consequence, the boundary is represented in a piecewise linear fashion.

Michell (1904) derived closed-form optimal structures for a variety of two-dimensional problems, with a single three-dimensional problem: The optimal structure to transfer a moment pair distributed over small circumferences with no constraint on the domain size (Fig. 1a). Michell's derivations did not include details, and the solution was later re-derived by Hemp (1973) and Lewiński (2004). The optimal solution resembles a hollow ball with curved mutually-orthogonal members on its surface as shown in Fig. 1b. The proposed method's capability to address unstructured non-orthogonal domains offers a reasonable numerical approximation to the analytical closed-form solution. The result obtained with the proposed algorithm is shown in Fig. 1c for comparison.

The limitations and assumptions of the present implementation are:

- single static load case scenario;
- constant forces (design independent);
- small deformations.

It can, however, address different limits in tension σ_T and compression σ_C (Sokół 2011).

Throughout this manuscript, the terms *truss member* and *bar* are used interchangeably. The manuscript is organized as follows: Section 2 briefly reviews the formulation used and its extension to three-dimensions. Section 3 provides details on the implementation of the method. The method and its implementation are verified against closed-form solutions in Section 4. Selected examples and their convergence are analyzed in Section 5. Conclusions and findings are summarized in Section 6. Appendix A has the nomenclature and symbols used in the manuscript. Finally, the derivations for the three-dimensional collision tests are given in Appendix B.

2 Formulations

This section briefly reviews the ground structure formulation based on plastic analysis. The reader can refer to Hemp

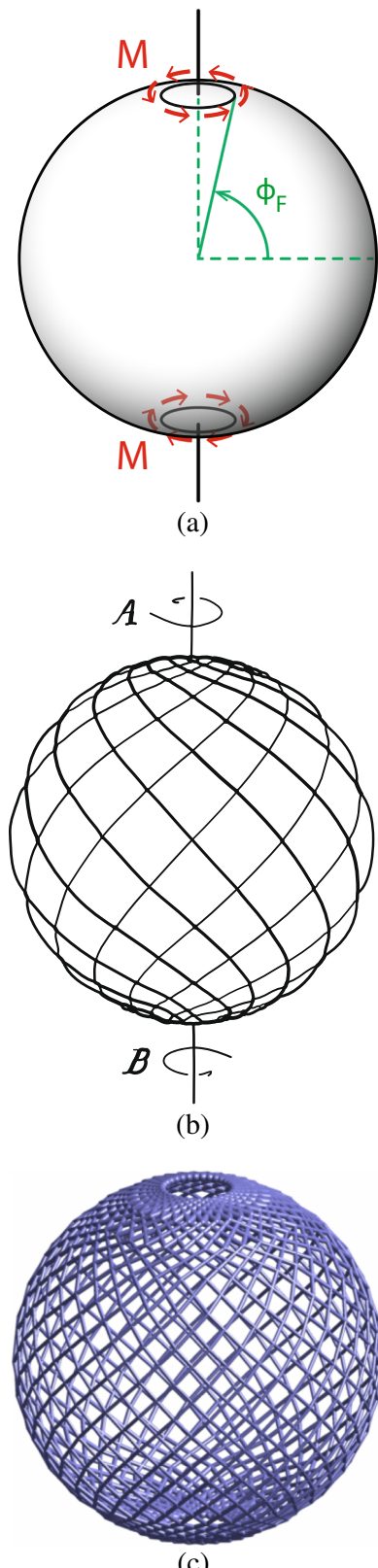
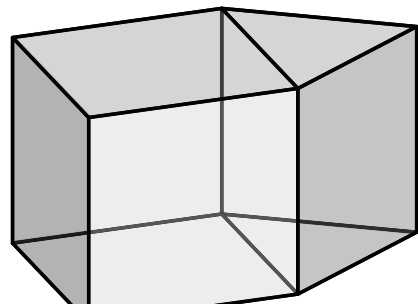


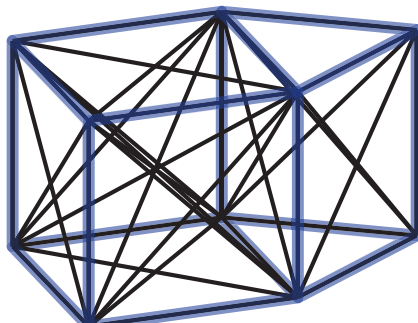
Fig. 1 Optimal structure to transfer a moment pair. **a** Domain and loads: The moments are distributed on equal rings at a latitude ϕ_F . **b** Analytical closed-form solution adapted from Michell (1904). **c** Numerical approximation obtained with GRAND3

(1973), Ohsaki (2010), Christensen and Klarbring (2009), and Gilbert and Tyas (2003) for additional details on the plastic and elastic versions of the method.

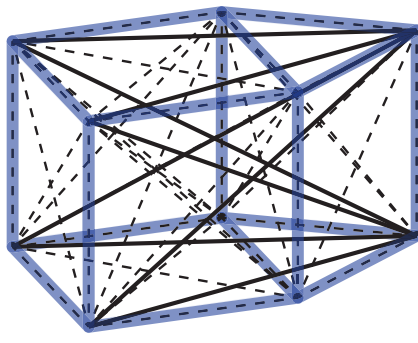
Consider a stable truss (no mechanisms), with N_{dof} nodal forces \mathbf{f} (excluding the components with supports), and assume that the supports are sufficient to prevent rigid



(a)



(b)



(c)

Fig. 2 Ground structure generation algorithm based on element connectivities. **a** Base mesh composed of a single hexahedron and a wedge. **b** Ground structure for level 1 connectivity: all nodes within an element are interconnected with bars. **c** Ground structure for level 2 connectivity: the new bars added at level 2 are plotted with solid lines

body motions. The minimum volume truss that satisfies the force equilibrium equations (plastic analysis) is (Hemp 1973; Ohsaki 2010):

$$\begin{aligned} \min_{\mathbf{a}} \quad & V = \mathbf{l}^T \mathbf{a} \\ \text{s.t.} \quad & \mathbf{B}^T \mathbf{n} = \mathbf{f} \\ & -\sigma_C a_i \leq n_i \leq \sigma_T a_i \quad i = 1, 2 \dots N_b, \end{aligned} \quad (1)$$

with V the truss' volume, a_i , l_i and σ_i the cross-sectional area, length and stress of the i th truss member (for all N_b members in the truss). The matrix \mathbf{B}^T is the nodal equilibrium matrix of size $N_{dof} \times N_b$, built from the directional cosines of the members, and \mathbf{n} is a vector with the internal (axial) force for all members in the ground structure. Theoretically, a member is absent (removed) from the truss if $a_i = 0$. The redundancy of the ground structure is $N_b - N_{dof}$ and should be greater than zero to provide multiple layout options. This formulation, based on *plastic analysis*, only enforces force equilibrium, i.e. the compatibility or stress-strain relations are not included (Kirsch 1993).

The stress constraint, either in tension or compression, must be active for all members at the optimum. This can be proven intuitively: if the i th member has $n_i < \sigma_T a_i$ and $n_i > -\sigma_C a_i$, then a_i can be reduced (reducing the total volume) without violating the constraints. Incorporating *slack variables* s^+ and s^- in the stress constraints (Hemp

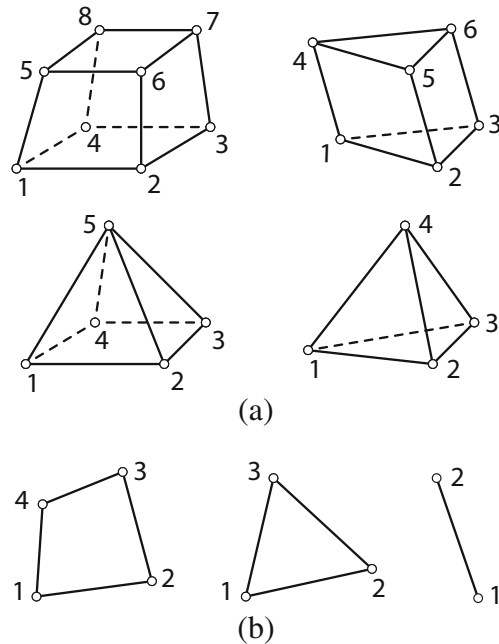


Fig. 3 Elements supported by GRAND3 and their corresponding node numbering scheme. **a** Volumetric elements: Hexahedron (8-nodes), Prism (6-nodes), Pyramid (5-nodes) and Tetrahedron (4-nodes). **b** Surface elements: Quadrangle (4-nodes), Triangle (3-nodes) and Segment (2-nodes)

1973; Achtziger 2007), the inequalities can be converted into equalities, and the optimization problem in (1) becomes a linear programming problem as:

$$\begin{aligned} \min_{s^+, s^-} \quad & V = \mathbf{I}^T \left(\frac{\mathbf{s}^+}{\sigma_T} + \frac{\mathbf{s}^-}{\sigma_C} \right) \\ \text{s.t.} \quad & \mathbf{B}^T (\mathbf{s}^+ - \mathbf{s}^-) = \mathbf{f} \\ & s_i^+, s_i^- \geq 0, \end{aligned} \quad (2)$$

with $a_i = s_i^+/\sigma_T + s_i^-/\sigma_C$ and $n_i = s_i^+ - s_i^-$. Note that for any active member, only one of s_i^+ and s_i^- is non-zero. The member is in tension if $s_i^+ > 0$, and in compression if $s_i^- > 0$. If the truss structure is stable and has no repeated or overlapping members, then the rank of matrix \mathbf{B}^T is N_{dof} (i.e. the solution lies on a corner of the feasible domain). The solution of the linear program in (2) yields at most N_{dof} non-zero *basic variables*, with the remainder *non-basic variables* absent from the optimal structure (i.e. $a_i = 0$). Therefore, the optimal truss is statically determinate and the solution is also globally optimal (Sved 1954; Kicher 1966): The optimal solution will automatically satisfy the kinematic compatibility and stress-strain relations (Dorn et al. 1964; Hemp 1973).

Table 1 Domain definition (base mesh) input requirements for GRAND; the provided implementation of the method

Variable Name	Type & Size	Description
NODE	array $N_n \times 3$	Each row p has the nodal coordinates x, y and z for node p .
ELEM	struct	Structure with fields V and/or S for <i>volumetric</i> and <i>surface</i> elements respectively. The numbering scheme is given in Fig. 3.
ELEM.V	cell $N_{ve} \times 1$	Entries are row vectors containing the node numbers for each particular <i>volumetric</i> element. The total number of volumetric elements is N_{ve} .
ELEM.S	cell $N_{se} \times 1$	Entries are row vectors containing the node numbers for each particular <i>surface</i> element. The total number of surface elements is N_{se} .
SUPP	array $N_f \times 4$	Each row consists of a node number, fixity x , fixity in y and fixity in z . Any value other than NaN specifies fixity. The total number of specified fixities is N_{sup} .
LOAD	array $N_l \times 4$	Each row consists of a node number, load in x , load in y and load in z . A zero or NaN specify no force in that direction.

Defining the stress limits ratio as $\kappa = \sigma_T/\sigma_C$ and using matrix notation, (2) can be rewritten as :

$$\begin{aligned} \min_{s^+, s^-} \quad & V^* = \frac{V}{\sigma_T} = \left\{ \mathbf{I}^T \kappa \mathbf{I}^T \right\}_{1 \times 2N_b} \left\{ \begin{array}{c} \mathbf{s}^+ \\ \mathbf{s}^- \end{array} \right\}_{2N_b \times 1} \\ \text{s.t.} \quad & \left[\mathbf{B}^T - \mathbf{B}^T \right]_{N_{dof} \times 2N_b} \left\{ \begin{array}{c} \mathbf{s}^+ \\ \mathbf{s}^- \end{array} \right\}_{2N_b \times 1} = \mathbf{f}_{N_{dof} \times 1} \\ & s_i^+, s_i^- \geq 0 \end{aligned} \quad (3)$$

The number of degrees-of-freedom (DOFs) is $N_{dof} = 3N_n - N_{sup}$, with N_n the number of nodes in the ground structure and N_{sup} the number of fixed (supported) degrees of freedom. The optimal volume V^* is calculated for $\sigma_T = 1$, and should be scaled by $1/\sigma_T$ for values other than unity. Equation (3) highlights the sizes of the variables involved. By introducing slack variables, the number of design variables in (3) is doubled compared to the number of design variables in (1). However, while (1) is a nonlinear program, (3) is a linear program and can be solved more efficiently

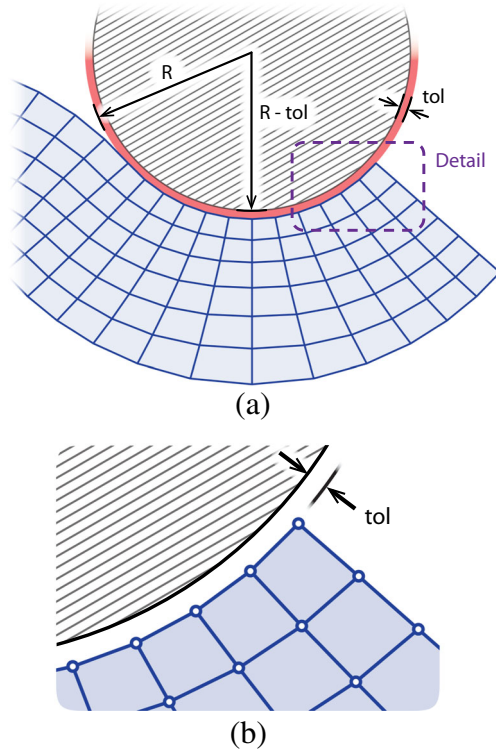
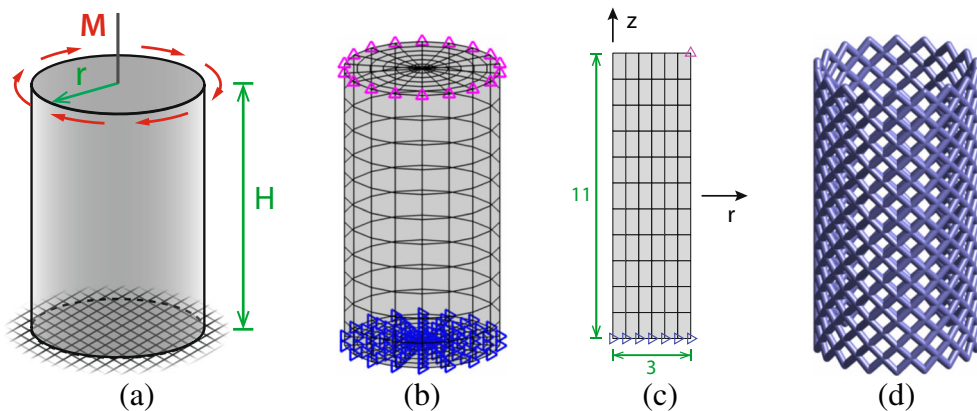


Fig. 4 Restriction zone setback: this user-defined setback is a margin of comparatively small size tol in order to ensure that the domain's nodes remain outside the restriction zones. **a** Example of the restriction zone for a domain with a circular concavity. The concavity radius is R , however the actual restriction zone applied is $R - tol$. **b** Detail of the restriction zone setback: the nodes on the domain's concave boundary (shown in the Figure) must remain clear of the restriction primitive

Fig. 5 Torsion cylinder problem. **a** Domain definition, loading and supports. **b** Sample mesh for $H = 11$, $r = 3$ discretized with $N_z = 11$, $N_r = 6$ and $N_\theta = 18$. **c** Axisymmetric plot of the sample mesh with $H = 11$, $r = 3$, $N_z = 11$ and $N_r = 6$. **d** Solution obtained for $N_b = 152,795$, generated from a cylindrical domain with $N_e = 1,188$, $N_n = 1,308$ and $Lvl = 3$



using the interior-point algorithm (Karmarkar 1984; Wright 2004). Problems with solutions that lie on a facet (or edge) of the feasible domain are called *degenerate*, and tend to be computationally more difficult to solve.

3 Implementation

The implementation is an extension of the two-dimensional GRAND (Zegard and Paulino 2014). The concepts and algorithms from the previous two-dimensional implementation are directly extended with a few exceptions that are detailed here.

3.1 Domain definition — Base mesh

The ground structure generation algorithm requires a base mesh from where to generate the nodal connectivity matrix. No edge, facet or volume information is needed from this base mesh—it is strictly used to obtain nodal connectivity information. The ground structure generation process begins by connecting all nodes within an element: this is referred as *level 1* connectivity. Take the 2 element mesh in

Fig. 2a for example (a hexahedron and a wedge element); the ground structure with a level 1 connectivity will generate bars between all the nodes belonging to an element, as shown in Fig. 2b. These nodes are direct neighbors of each other based on the element connectivity provided by the mesh. At level 2, the proposed method will generate bars up to the *neighbors or my neighbors*, therefore including level 1 bars. The (new) bars at level 2, will traverse 2 elements in the base mesh as shown in Fig. 2c. The generated ground structure will become more redundant and dense with each connectivity level. The method can use any base mesh provided that it is built from convex polytopes; this because at level 1, all nodes within an element are connected regardless. While the elements in the base mesh need to be convex, the mesh itself does not. This and other details on the ground structure generation are addressed in Section 3.2.

The fact that no edge or facet information is provided can prove to be challenging for plotting routines if complicated convex polytopes are given. In addition, the maturity of 3D polytope meshing algorithms (Barber et al. 1996; Herceg et al. 2013; Rycroft 2014) is lagging behind that of more traditional meshing algorithms based on standard elements

Table 2 Convergence for a cylinder under torsion with $M = 5$, $H = 11$ and $r = 3$

N_z	N_r	N_θ	N_e	N_n	N_b	Volume V
7	4	12	336	392	32,911	37.9628
9	5	15	675	760	78,954	37.4937
11	6	18	1,188	1,308	152,795	37.2637
13	7	22	2,002	2,170	278,467	37.0453
15	8	26	3,120	3,344	458,811	36.9395
17	9	29	4,437	4,716	677,370	36.8830
19	10	32	6,080	6,420	950,419	36.8486

Ground structures are generated with $Lvl = 3$. The optimal volume is $V_{opt} = 36.6667$

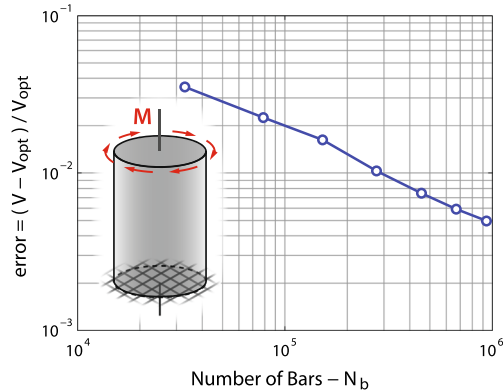


Fig. 6 Convergence for the cylinder problem with base mesh refinement

Fig. 7 Torsion cone problem. **a** Domain definition, loading and supports. **b** Sample mesh for $H = 10$, $r_L = 7$ and $r_U = 2$ discretized with $N_z = 9$, $N_r = 5$, $N_\theta = 20$ and $\lambda = 0.870058$. **c** Axisymmetric plot of the sample mesh with $H = 10$, $r_L = 7$, $r_U = 2$, $N_z = 9$, $N_r = 5$ and $\lambda = 0.870058$. **d** Solution obtained for $N_b = 115, 789$, generated using a discretization in cylindrical coordinates with $N_e = 900$, $N_n = 1,010$ and $Lvl = 3$

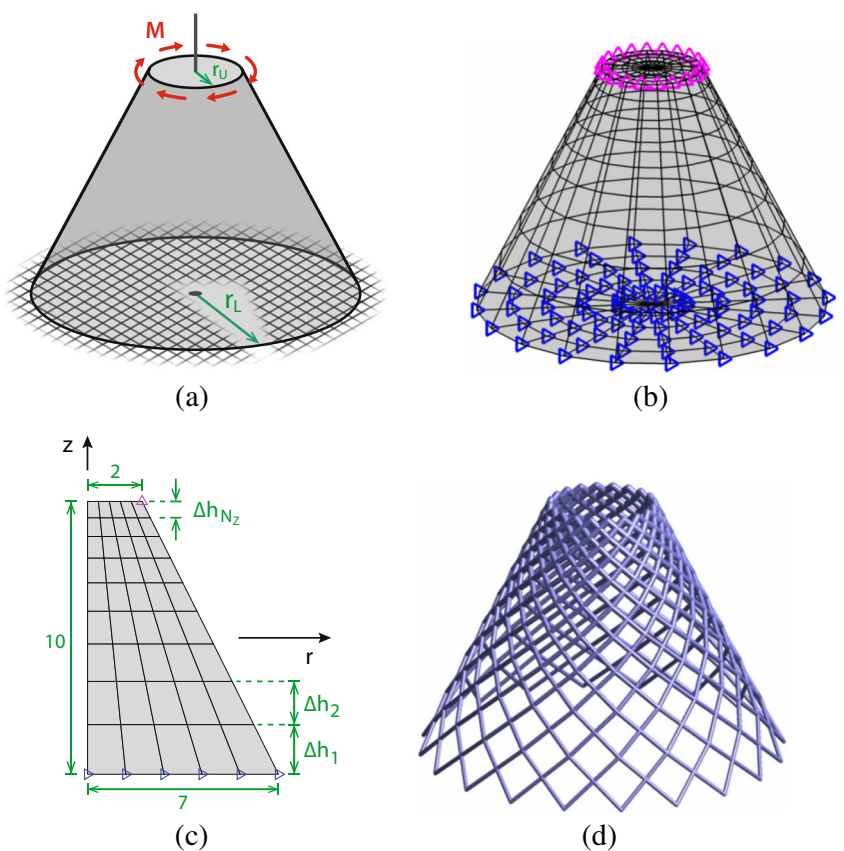


Table 3 Convergence for a capped cone under torsion with $M = 3$, $H = 10$, $r_L = 7$ and $r_U = 2$

N_z	N_θ	λ	N_e	N_n	N_b	Volume V
5	9	0.778371	225	276	22,532	18.2822
6	12	0.811563	360	427	38,946	17.5218
7	15	0.836134	525	608	61,072	17.2178
8	17	0.855050	680	774	82,849	17.1354
9	20	0.870058	900	1,010	115,789	17.0310
10	22	0.882253	1,100	1,221	147,058	16.9935
11	25	0.892358	1,375	1,512	193,686	16.9526
12	27	0.900868	1,620	1,768	235,938	16.9300
13	30	0.908131	1,950	2,114	296,383	16.9146
14	32	0.914404	2,240	2,415	350,830	16.8982
15	35	0.919875	2,625	2,816	429,220	16.8947
16	37	0.924689	2,960	3,162	497,407	16.8813
17	40	0.928958	3,400	3,618	592,377	16.8837
18	42	0.932769	3,780	4,009	675,462	16.8720
19	45	0.936192	4,275	4,520	792,874	16.8776
20	47	0.939283	4,700	4,956	892,456	16.8670

Ground structures are generated with $N_r = 5$ and $Lvl = 3$. The optimal volume is $V_{opt} = 16.8076$

(hedrahedra, tetrahedra, wedges, etc). Therefore, while the algorithm for ground structure generation and analysis can address any element type in the base mesh, for practical purposes, the current implementation is limited to 7 simple elements: 4 volumetric and 3 surface elements (the segment, although not flat, is grouped with surface elements). The 7 elements supported in the current implementation are illustrated in Fig. 3.

These elements have a unique topology (facets and edges), provided that they are numbered properly. The surface elements are not two-dimensional, but three-dimensional entities that can be used to define shells, domes and membranes for example. The segment element is special: it can be used to fine-tune the nodal connectivity matrix by allowing two non-neighboring nodes to share level 1 connectivity.

The input specification for the base mesh, supports and loads for the provided implementation, is detailed in Table 1. The ELEM variable is a structure (or *struct*) with fields V and S for volumetric and surface elements respectively. The analysis can comprise volumetric, surface or a combination of elements in the base mesh. In other words, at least one field in ELEM must be defined (V or S). The total number of volumetric and surface elements are N_{ve} and N_{se} respectively. Therefore, the total number of elements in the base mesh is $N_e = N_{ve} + N_{se}$.

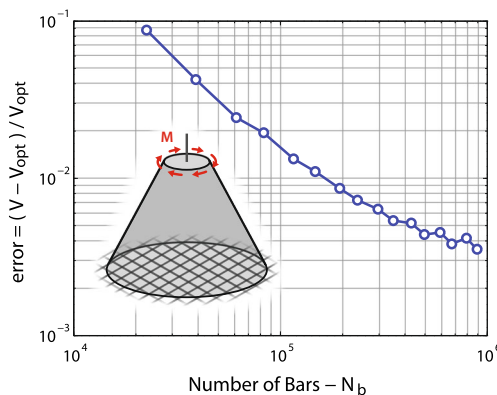
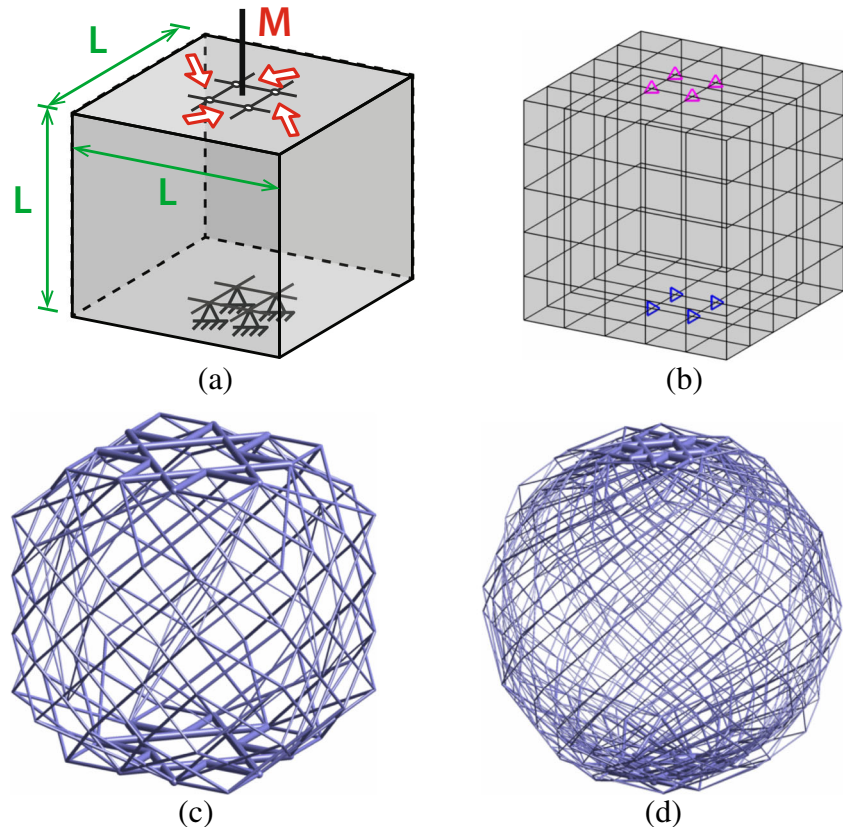


Fig. 8 Convergence for the cone problem with base mesh refinement

3.2 Ground structure generation

The ground structure generation follows the procedure outlined in the two-dimensional implementation (Zegard and Paulino 2014). The *connectivity level* parameter (*Lvl*) indirectly controls the level of redundancy, or interconnectedness, of the initial ground structure (refer to Fig. 2). Two nodes are considered *neighbors* and share level 1 connectivity if they belong to the same element in the base mesh. From this idea of neighbors, the connectivity level can be explained as follows:

Fig. 9 Torsion ball problem modeled using an orthogonal domain. **a** Domain definition, loading and supports. **b** Sample mesh with $N = 5$. **c** Optimal structure obtained with $N = 5$, $Lvl = 4$ and $N_b = 15,980$. **d** Optimal solution obtained with $N = 13$, $Lvl = 4$ and $N_b = 475,996$



- Level 1 connectivity will generate members between all neighboring nodes.
- Level 2 connectivity will generate members up to the neighbors of the neighbors.
- Level 3 connectivity will generate members up to the neighbors of the neighbors of the neighbors.

This process scales rapidly and only decelerates when the member generation is reaching full connectivity throughout the domain. The nodal connectivity matrix for level 1, \mathbf{A}_1 , is built from the base mesh and is defined as follows:

$$[\mathbf{A}_1]_{p,q} = \begin{cases} 1 \text{ or } \text{true} & \text{if nodes } p, q \text{ share an element} \\ 0 \text{ or } \text{false} & \text{otherwise or if } p = q \end{cases}, \quad (4)$$

resulting in a symmetric \mathbf{A}_1 , i.e. bi-directional.

The second level connectivity can be obtained as $\mathbf{A}_2 = \mathbf{A}_1 \mathbf{A}_1 = [\mathbf{A}_1^2]$. However, some entries may well be > 1 and have values other than zero in the diagonal. Therefore, the nodal connectivity matrix for levels $n > 1$ is then:

$$[\mathbf{A}_n]_{p,q} = \begin{cases} 0 \text{ or } \text{false} & \text{if } [\mathbf{A}_1^n]_{p,q} = 0 \text{ or if } p = q \\ 1 \text{ or } \text{false} & \text{if } [\mathbf{A}_1^n]_{p,q} > 0 \text{ and } p \neq q \end{cases} \quad (5)$$

The new bars for level n can be obtained as:

$$\mathbf{G}_n = \mathbf{A}_n - \mathbf{A}_{n-1}, \quad (6)$$

Table 4 Convergence for a regular orthogonal domain of side $L = 1$ under torsion with $M = 1$

Base mesh	N	N_e	N_h	R	ϕ_F	Lvl	N_b	V_{opt}	Volume V
very coarse	5	125	216	0.5196	1.2952	2	5,540		9.6571
						3	11,372	7.9017	9.6571
						4	15,980		9.6571
						5	19,508		9.6571
coarse	7	343	512	0.5101	1.3714	2	15,652		10.8069
						3	35,932	9.2101	10.8069
						4	56,668		10.8069
						5	82,804		10.8069
mid-coarse	9	729	1,000	0.5061	1.4149	2	33,804		11.8774
						3	82,356	10.1997	11.8615
						4	137,652		11.8615
						5	218,652		11.8615
mid-fine	11	1,331	1,728	0.5041	1.4429	2	62,348		12.6330
						3	157,604	10.9943	12.6252
						4	272,804		12.6252
						5	454,748		12.6252
fine	13	2,197	2,744	0.5029	1.4624	2	103,636		13.3360
						3	268,636	11.6579	13.3041
						4	475,996		13.3015
						5	818,788		13.3015
very fine	15	3,375	4,096	0.5022	1.4768	2	160,020		13.9097
						3	422,412	12.2274	13.8713
						4	761,100		13.8649
						5	1,338,468		13.8642

where \mathbf{G}_n has non-zero entries for the bars generated at level n (note that $\mathbf{G}_1 = \mathbf{A}_1$). The new bars obtained from \mathbf{G}_n are considered *candidate* bars: they still need to pass the collinearity and restriction zone checks (Sections 3.3 and 3.4 respectively) to be included in the final ground structure.

The number of bars, and therefore the number of variables in the optimization problem, grow rapidly with an increase of the connectivity level. In general, it is not recommended to use high values for the *connectivity level*; i.e. connect nodes that are far away from each other. The analytical closed-form solutions are typically composed of curved members (Michell 1904; Lewiński 2004). The method can better approximate these curved-member solutions with many short bars in a piecewise fashion, as opposed to the long members that result from a high connectivity level.

3.3 Collinearity check

The collinearity (or overlapping) member check assumes the following:

1. New bars added at level n are deleted if found collinear with bars from previous levels.
2. New bars added at level n are assumed not to be collinear between them. They are only checked for

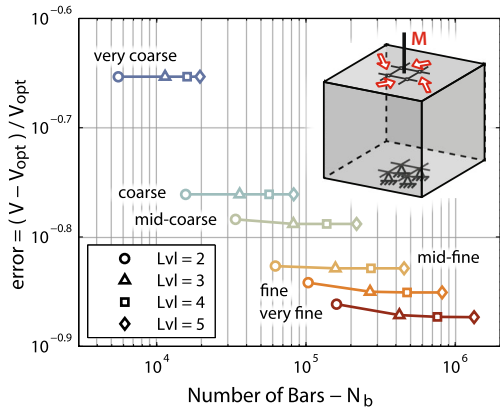


Fig. 10 Convergence to the optimal solution of increasingly refined regular orthogonal base meshes under torsion. For this problem, increasing the ground structure connectivity level does have much impact on the quality of the solution

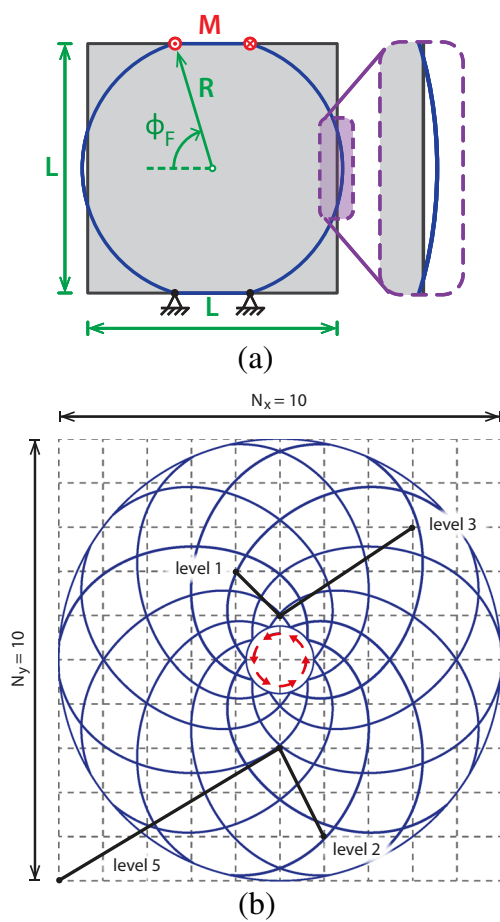


Fig. 11 Sources of poor accuracy and convergence for the torsion ball problem approximated with a regular structured-orthogonal cube mesh of dimension L . **a** A cube domain is not able to accommodate the optimal solution. The radius of the (optimal) sphere R is larger than half of the domain's width $L/2$ (refer to (13)). **b** Polar view of the analytical closed-form solution for the torsion ball problem. A fictitious regular discretization with some members is shown to highlight the inability of higher level members to approximate the solution

collinearity against previously generated bars (not to each other).

In general, new bars are *longer* than those generated at lower connectivity levels, thus justifying the decision to eliminate the newly generated bar as opposed to the previously accepted one. The second assumption may be violated if the base mesh has elements that are not strictly convex, although most meshing algorithms will generate meshes with strictly convex elements. More uncommonly, as the ground structure for higher levels is generated, the algorithm expansion may reach two collinear nodes at a single step: this unlikely situation may occur in domains that curl or spiral around themselves and is generally not a concern within the scope of this work.

The length of a member spanning between nodes p and q with coordinates $\{x_p, y_p, z_p\}$ and $\{x_q, y_q, z_q\}$ is defined as:

$$L_{p,q} = \sqrt{(x_q - x_p)^2 + (y_q - y_p)^2 + (z_q - z_p)^2} \quad (7)$$

The directional cosines vector for the bar between nodes p and q is $\hat{\mathbf{d}}_{p,q}$:

$$\hat{\mathbf{d}}_{p,q} = \frac{\{x_q - x_p, y_q - y_p, z_q - z_p\}}{L_{p,q}} \quad (8)$$

Note that the bar length and directional cosines are also used in the formulation of the ground structure optimization problem (3).

Once \mathbf{G}_n is obtained, the new (candidate) bars must be checked not to be collinear with members already in the ground structure. A candidate bar \overline{pq} is rejected due to collinearity if it has a small-enough angle with a previously

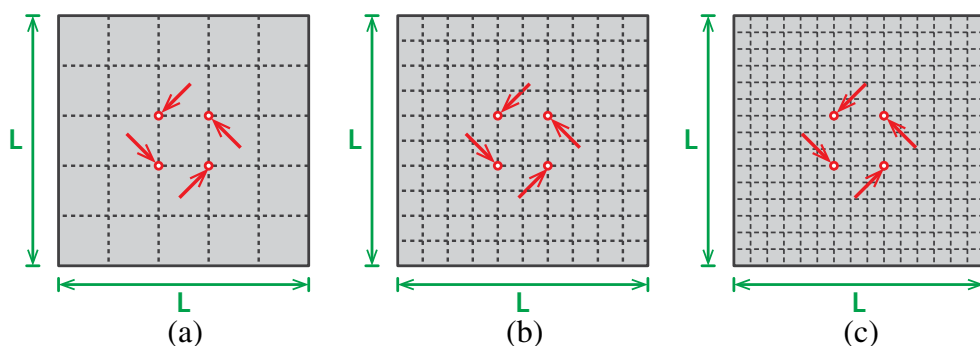


Fig. 12 Top view of the orthogonal domains used in approximating the torsion ball problem, while maintaining a constant angle ϕ_F . **a** Domain discretized into $N = 5$ elements in each direction. **b**

Domain discretized into $N = 10$ elements in each direction. **c** Domain discretized into $N = 15$ elements in each direction

Table 5 Convergence for the torsion ball problem in an orthogonal domain, with constant moment application latitude ϕ_F

N	N_e	N_n	N_b	V
5	125	216	11,372	9.6571
10	1,000	1,331	115,942	8.9952
15	3,375	4,096	422,412	8.7077
20	8,000	9,261	1,039,532	8.6064

The solution is approximated with a cube domain of size $L = 1$, partitioned into $N \times N \times N$ elements, using $Lvl = 3$, loaded (and supported) at 4 points near the poles, with $M = 1$, $\phi_F = 1.2952$, $R = 0.5196$ and $V_{opt} = 7.9017$

accepted bar in the ground structure. The angle between bars is checked using the dot product of the directional cosines¹:

$$\begin{cases} \text{accept bar } \overline{pq} \text{ if } \hat{\mathbf{d}}_{p,q} \cdot \hat{\mathbf{d}}_{p,i} < \text{ColTol} & \forall i \\ \text{reject bar } \overline{pq} & \text{otherwise} \end{cases} \quad (9)$$

The user-defined $\text{ColTol} \lesssim 1$ controls the admissible collinearity between members: the minimum angle between generated bars is $\alpha \geq \arccos(\text{ColTol})$. Additional details (with examples) on the collinearity check can be found in Zegard and Paulino (2014).

3.4 Restriction zones

Analogous to the two-dimensional implementation of the method, the restriction zone idea is inspired by known collision detection algorithms used in video-games and in computational geometry (Ericson 2004).

The domain may have concave regions or holes that no bar should intersect. To prevent the ground structure generation algorithm from laying out members in these regions, the user defines *restriction zones* (i.e. hitboxes): geometric entities that no bar should intersect. The current implementation of GRAND3 provides the following restriction primitives:

- box
- cylinder
- disc
- quadrangle (flat)
- rod (finite cylinder)
- sphere
- triangle (flat)
- surface²

¹A directional cosine vector has a norm of unity by definition, and thus the dot product of directional cosines vectors is equal to the cosine of the angle between them.

²This collision primitive is built from multiple calls to the triangle and quad collision primitives.

These primitives can be combined to create complicated regions or boundaries, and the user can easily implement new collision primitives in GRAND3. The derivation and details on these primitives are given in Appendix B.

Nodes in the base mesh must not intersect the restriction zones nor its boundary. If this happens, then all bars originating from such node will be flagged for removal during the restriction zone check. Thus, a small reduction in size of the restriction primitives is advised. This setback (or margin) is in the form of a small tolerance tol as shown in Fig. 4. The setback distance tol is defined by the user when defining the restriction zones, and should be relative to the scale of the problem.

The ground structure generation, after the collinearity and restriction zone checks, returns a list of (accepted) bars (or members). This process operates over symmetric (or bi-directional) matrices. However, to prevent duplicate members, only bars \overline{pq} with $p < q$ are reported.

4 Verification

The following examples aim to verify GRAND3 by approximating optimal closed-form solutions. Members with cross-sectional area $a_i < (\text{Cutoff}) \max(\mathbf{a})$ (a) are not plotted. Unless otherwise stated, the stress limit ratio is $\kappa = 1.0$ with $\sigma_T = 1$, the collinear tolerance is $\text{ColTol} = 0.999999$ and the plotting cutoff is $\text{Cutoff} = 0.005$.

4.1 Torsion cylinder

A cylindrical domain of radius r and height H is subjected to an end moment distributed over the outer ring of the upper end cap (Fig. 5a). The domain is fully supported on the bottom end cap. This problem is of interest since the analytical volume for the theoretical optimal structure can be derived.

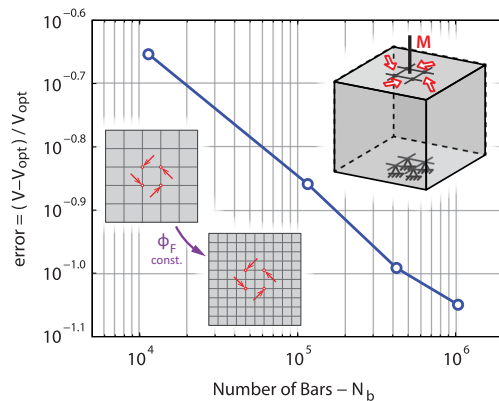


Fig. 13 Convergence to the optimal solution of increasingly refined regular orthogonal base meshes under torsion, while maintaining the moment application latitude ϕ_F constant

A moment pair causes a pure-shear condition on the cylinder surface. Therefore, the principal stress lines are oriented at $\pm\pi/4$. The members in the optimal solution must follow the lines of principal stresses (Michell 1904; Hencky 1923; Hemp 1973). A single fiber following a principal stress line has a length $l_f = \sqrt{2}H$. The force in the fiber due to the moment pair is $n_f = \sqrt{2}M/4\pi r^2$ for tension, and $-n_f$ for compression. Finally, the volume of the optimal cylinder in torsion is:

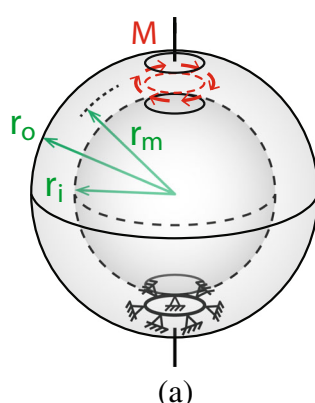
$$\begin{aligned} V_{opt} &= \left[\frac{(n_f)(l_f)}{\sigma_T} - \frac{(-n_f)(l_f)}{\sigma_C} \right] (2\pi r) \\ &= \left(\frac{\sqrt{2}M}{4\pi r^2} \right) (\sqrt{2}H) \left[\frac{1}{\sigma_T} + \frac{1}{\sigma_C} \right] (2\pi r) \\ &= \frac{MH}{r} \left[\frac{1}{\sigma_T} + \frac{1}{\sigma_C} \right] \end{aligned} \quad (10)$$

Using cylindrical coordinates, the model is discretized in $N_z \times N_r \times N_\theta$ elements corresponding to the z , r and θ coordinate axes respectively. The problem is analyzed for the specific case where $H = 11$, $r = 3$ and $M = 5$. A sample mesh discretized with $\{N_z, N_r, N_\theta\} = \{12, 6, 16\}$ is shown in Fig. 5b. An axisymmetrical plot of this mesh is given in Fig. 5c. One of the solutions obtained with the proposed method is plotted in Fig. 5d as an example. The convergence of the ground structure method with refinement of the base mesh is given in Table 2 and Fig. 6. There is a convergence towards the optimal volume $V_{opt} = 36.6667$.

4.2 Torsion cone

A capped cone domain of height $H = 10$ with lower and upper radius $r_L = 7$ and $r_U = 2$ respectively, is subjected to an end moment $M = 3$ distributed over the outer ring at the upper end cap (Fig. 7a). The analytical solution for this

Fig. 14 Torsion ball problem. **a** Domain definition, loading and supports. **b** Sample mesh with $r_i = 2.9$, $r_m = 3$ and $r_o = 3.1$ discretized with $N_\theta = 30$, $N_\phi = 14$ and $N_r = 2$. **c** Axisymmetrized plot of the sample mesh with $\pi/2 - \phi_F = \pi/10$, $r_i = 2.9$, $r_m = 3$ and $r_o = 3.1$ discretized with $N_\phi = 14$ and $N_r = 2$



problem was derived by Lewiński (2004), by constraining the solution to exist in the cone's surface:

$$V_{opt} = M \frac{\sqrt{H^2 + (r_L - r_U)^2}}{r_L - r_U} \log \left(\frac{r_L}{r_U} \right) \left[\frac{1}{\sigma_T} + \frac{1}{\sigma_C} \right], \quad (11)$$

that for the specific geometry and loads being considered results in $V_{opt} = 16.8076$.

Using cylindrical coordinates, the model is discretized in $N_z \times N_r \times N_\theta$ elements corresponding to the z , r and θ coordinate axes respectively. An axisymmetrized plot of this mesh is given in Fig. 7c. In an effort to preserve the aspect ratio of the elements in the mesh, the spacing in the z direction is such that $\Delta h_{i+1}/\Delta h_i = \lambda$, with λ being constant. A sample mesh discretized with $\{N_z, N_r, N_\theta\} = \{9, 5, 20\}$ and $\lambda = 0.87006$ is shown in Fig. 7b. One of the solutions obtained with the proposed method is plotted in Fig. 7d as an example. The convergence of the ground structure method with refinement of the base mesh is given in Table 3 and Fig. 8. The increasingly refined solutions converge smoothly toward the optimum, with a relatively small oscillation appearing when the number of bars is $N_b > 400,000$. The reason behind this oscillation being that the node positions do not precisely match the locations dictated by the analytical closed-form solution; i.e. the height is not a multiple of π . The quality of the approximation will therefore depend on the aspect ratio of the elements in the base mesh, as defined by N_z , N_θ and λ . However, the overall trend does converge to the analytical optimum as expected.

4.3 Torsion ball (orthogonal domain)

The optimal structure for transmitting a torsion pair is a *ball*, provided that the domain is large enough to allow the full solution to develop (Fig. 1b). In contrast, the torsion cylinder (Section 4.1) addresses a similar problem but with a constrained domain. With no previous knowledge of the

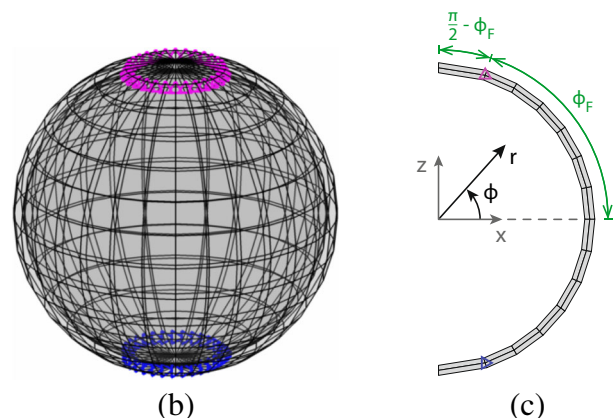


Table 6 Convergence for a hollow spherical domain with $M = 7$, $r_i = 2.9$, $r_m = 3.0$ and $r_o = 3.1$

N_θ	N_ϕ	N_e	N_n	N_b	ϕ_F	V_{opt}	Volume V
16	8	256	342	4,308	1.1781	45.2170	48.5088
24	12	576	798	21,076	1.3090	56.7725	60.2254
32	16	1,024	1,446	59,780	1.3744	64.8980	67.9621
40	20	1,600	2,286	121,244	1.4137	71.1785	74.0993
48	24	2,304	3,318	202,036	1.4399	76.3012	78.9887
56	28	3,136	4,542	308,844	1.4586	80.6280	83.4937
64	32	4,096	5,958	425,284	1.4726	84.3738	87.6053
72	36	5,184	7,566	575,932	1.4835	87.6764	91.4038

The discretization in ϕ is constant; i.e. the angle ϕ_F (and the volume V_{opt}) increases with refinement. Ground structures are generated with $N_r = 2$ and $Lvl = 3$

optimal solution, it is reasonable to use a regular and orthogonal base mesh. The moment (and support) is applied at the four nodes closest to the poles, as shown in Fig. 9a and b.

The optimal volume for this problem was obtained by Michell (1904), but a detailed derivation was not given. The solution for the torsion ball was later re-derived (Hemp 1973; Lewiński 2004) and confirmed.³ The optimal volume of the torsion ball is:

$$V_{opt} = 2M \log \left(\tan \left\{ \frac{\pi}{4} + \frac{\phi_F}{2} \right\} \right) \left[\frac{1}{\sigma_T} + \frac{1}{\sigma_C} \right], \quad (12)$$

where ϕ_F is the *latitude* of the small rings where the moment is applied (Fig. 14a). It should be noted that the optimal volume is independent of the sphere's radius R . Nonetheless, the domain must be large enough to allow the solution's sphere with radius R to develop.

The problem domain considered has $L = 1$ and $M = 1$, and is discretized regularly into $N \times N \times N$ elements. Sample solutions obtained for two different discretizations are shown in Fig. 9c and d. The convergence of the ground structure method for increasingly refined base meshes is given in Table 4 and Fig. 10. Because the problem considers applying the loads and supports at the four nodes closest to the poles, this distance will decrease with refinement, i.e. the angle ϕ_F will increase as the element size in the base mesh decreases (Fig. 14c). Thus, the optimal volume V_{opt}

changes with the discretization. For a regular structured-orthogonal cube mesh of dimension L , discretized with N elements in each direction (Fig. 9), the angle ϕ_F is:

$$\begin{aligned} dx &= \frac{L}{N} \\ r_F &= \frac{1}{2} \sqrt{dx^2 + dx^2} = \frac{\sqrt{2}L}{2N} \\ \phi_F &= \text{atan} \left(\frac{L/2}{r_F} \right) = \text{atan} \left(\frac{\sqrt{2}N}{2} \right) \\ R &= \sqrt{\left(\frac{L}{2} \right)^2 + r_F^2} = \frac{L}{2N} \sqrt{N^2 + 2}, \end{aligned} \quad (13)$$

where dx is the dimension of a single hexahedral element in the base mesh, r_F is the distance from the pole to the loaded nodes (radius of the moment application ring), and R is the radius of the (optimal) sphere.

The poor convergence rate observed with mesh refinement, and even worse with connectivity level, is attributed to a number of reasons:

- This is a particularly unfavourable scenario for the method: approximating a sphere with a *box*.
- The load and supports are applied at four discrete locations as opposed to continuously throughout the ring.
- Increasing ϕ_F (equivalent to reducing the radius of the ring where the moment is applied), makes the problem more difficult to approximate numerically. Truss elements, cannot equilibrate a moment applied at a single point, and thus as $\phi_F \approx \pi/2$ the optimal volume $V_{opt} \rightarrow \infty$ (refer to (12)).
- The radius of the (optimal) sphere R (13), exceeds the boundaries of the domain⁴, i.e. $2R > L = 1$. Thus, the

³Michell's formula matches the subsequent work provided that the quantity L in Michell (1904) is taken to be equal to Mr . Whether Michell meant this to be the real meaning of the quantity L , or not, is unclear.

domain does not fully accommodate the optimal analytical solution (refer to the values of R given in Table 4). This situation, however, improves with mesh refinement due to an increase in ϕ_F (see Fig. 11a).

- For this problem in particular, the theoretical optimal solution is comprised solely of curved members. A high connectivity level will generate longer straight members, which do not improve the approximation for this analytical solution. Figure 11b shows the analytical solution viewed from the poles, along with a fictitious discretization illustrating some members at different connectivity levels: lower level members (shorter) have a better chance at approximating the solution.
- The method is discrete, and therefore sensitive to the shape and level of the discretization.
- Finite computational precision, inherent nature of a numerical optimizer, and tolerance parameters used.

4.4 Torsion ball (orthogonal domain) with constant moment latitude ϕ_F

Again using an orthogonal box domain as in the previous example, the error coming from an increase in ϕ_F can be eliminated. Starting with a domain discretized as in Fig. 12a, the mesh can be refined while keeping the locations of the loads and supports fixed as shown in Fig. 12b and c. For a level 3 connectivity, the convergence in this case is shown in Table 5 and Fig. 13. While there is an improvement in the results, these are not yet satisfactory: the optimal solution, a sphere, is discretized and approximated by a box, is a naïve initial guess for this problem, but likely to be made with no a priori knowledge of the solution.

4.5 Torsion ball (spherical domain)

Once knowledge is gained that the solution lies in a close-to-spherical domain, the base mesh can be modified to provide a better approximation. The base mesh in this case is a thick hollow sphere. This is not a shell, for it allows the solution to modify its radii if needed. The load is applied at an intermediate radius r_m between the inner and outer radii of the hollow sphere, r_i and r_o respectively, as shown in Fig. 14a. The domain is represented using spherical coordinates, and is discretized in the θ , ϕ and r directions using N_θ , N_ϕ and N_r elements respectively. A sample mesh

⁴This could be solved by making the domain wider than it is taller ($L_x = L_y > R$), but that would imply a priori knowledge of the solution.

Table 7 Convergence for a hollow spherical domain with $M = 7$, $r_i = 2.9$, $r_m = 3.0$ and $r_o = 3.1$

N_θ	N_ϕ	N_e	N_n	N_b	Volume V
20	10	400	546	10,564	54.9909
30	14	840	1,176	38,734	53.6278
40	18	1,440	2,046	96,484	52.8693
50	22	2,200	3,156	178,804	52.4600
60	26	3,120	4,506	283,444	52.2877
70	30	4,200	6,096	415,664	52.1777

The discretization in ϕ makes the first and last $\Delta\phi$ equal to $\pi/10$, with the remaining elements evenly distributed; i.e. the angle ϕ_F is constant and equal to $\phi_F = \pi/2 - \pi/10$ for all discretizations. Ground structures are generated with $N_r = 2$ and $Lvl = 3$. The optimal volume is $V_{opt} = 51.5964$

discretized with $\{N_\theta, N_\phi, N_r\} = \{30, 14, 2\}$ is shown in Fig. 14b, with an axisymmetrical plot given in Fig. 14c. The sphere is hollow, and thus a spherical restriction zone with radius r_i is used.

If the domain is discretized with a constant spacing on ϕ , then the angle ϕ_F of the applied force is:

$$\phi_F = \frac{\pi}{2} \frac{N_\phi - 2}{N_\phi} \quad (14)$$

The optimal volume, given by (12), will increase with refinement on the base mesh due to an increase in ϕ_F . Optimal volumes for increasingly refined base meshes with constant spacing in ϕ are given in Table 6.

In order to fix the latitude of the applied loads ϕ_F , the size of the first and last element on the ϕ partition are fixed, and the remaining elements are evenly distributed. Thus making ϕ_F constant for all discretizations (Fig. 14c), and consequently V_{opt} constant regardless of the refinement in

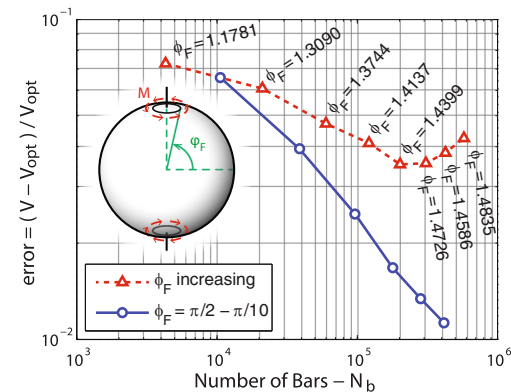
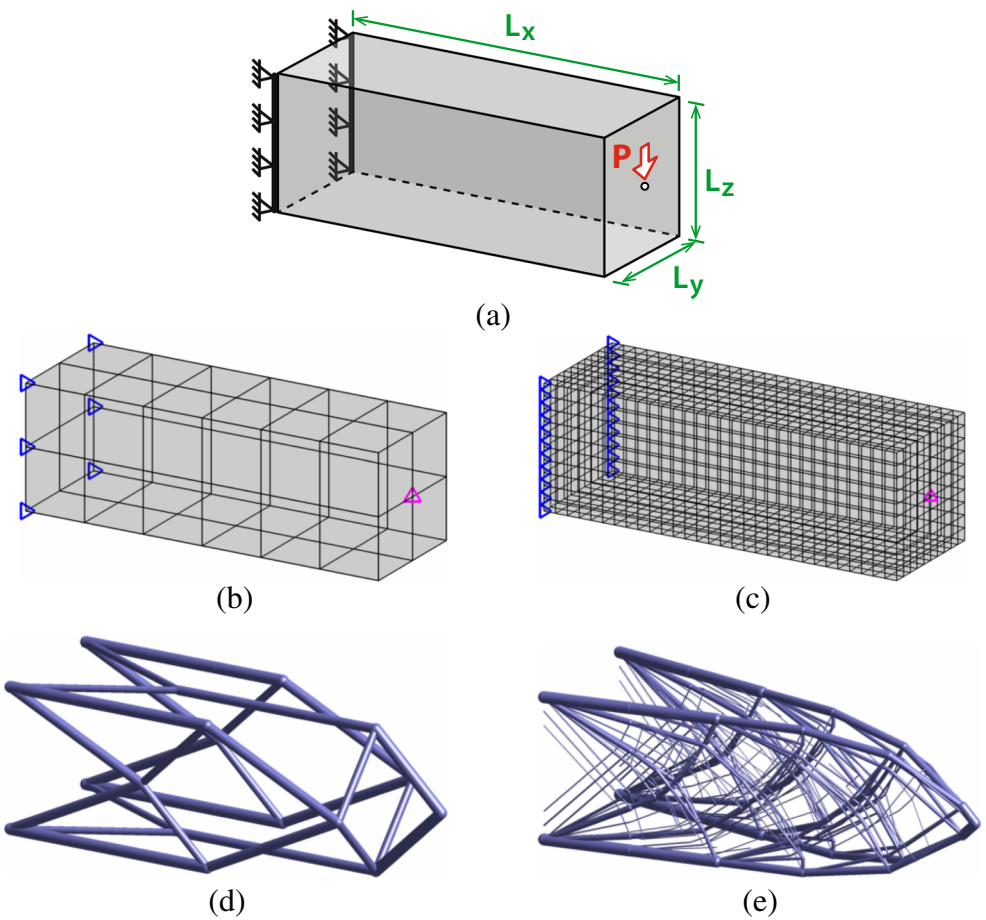


Fig. 15 Convergence to the optimal solution of increasingly refined spherical base meshes. The case where ϕ_F increases with refinement begins to diverge as $\phi_F \approx \pi/2$. The case where ϕ_F is constant converges as expected

Fig. 16 Edge-supported double cantilever problem. **a** Domain with loads, boundary conditions and dimensions. **b** Base mesh used to generate a coarse ground structure: $L_x = 3$, $L_y = L_z = 1$ and $P = 1$, discretized with $N_x = 6$ and $N_y = N_z = 2$, resulting in $N_e = 24$ and $N_n = 63$. **c** Base mesh used to generate a fine ground structure: $L_x = 3$, $L_y = L_z = 1$ and $P = 1$, discretized with $N_x = 30$ and $N_y = N_z = 10$, resulting in $N_e = 3,000$ and $N_n = 3,751$. **d** Solution for a coarse base mesh with $Lvl = 2$ and $N_b = 962$. **e** Solution for a fine base mesh with $Lvl = 6$ and $N_b = 1,474,218$



the base mesh. Taking $\pi/2 - \phi_F = \pi/10$, the analytical optimal volume is $V_{opt} = 51.5964$. The optimized volumes for increasingly refined base meshes are given in Table 7, with one of these solutions previously shown in Fig. 1c.

Making ϕ_F constant ensures that the refinement is approximating the same boundary value problem, and thus a smooth convergence to the analytical closed-form solution

is obtained. If ϕ_F is variable, then the method is approximating a different problem with each discretization, and thus convergence is not guaranteed. The torsion ball problem becomes more difficult to approximate numerically if the radius where the moment couple is applied is small (large ϕ_F). Convergence curves for both cases, variable and constant ϕ_F , are shown in Fig. 15.

Fig. 17 Edge-supported double cantilever problem with improved base mesh discretization. **a** Base mesh used to generate the ground structure: discretized with $N_x = 5$ and $N_y = N_z = 10$, resulting in $N_e = 1,000$ and $N_n = 726$. **b** Solution using the improved base mesh with $Lvl = 6$ and $N_b = 137,877$. The resulting optimal volume is $V = 14.2725$

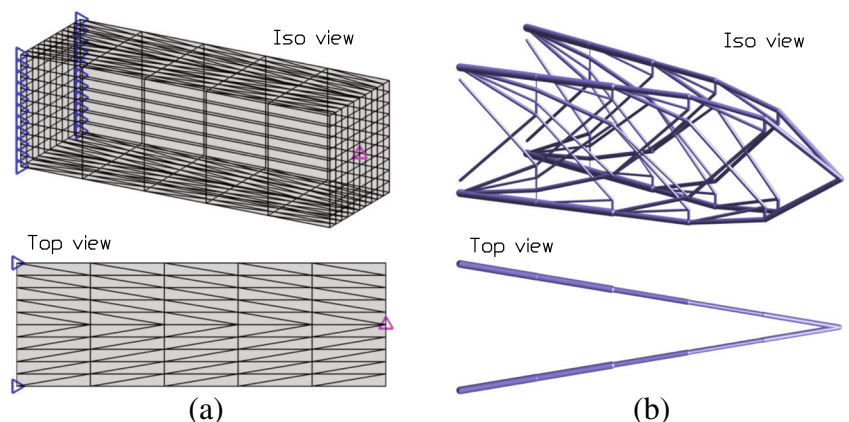


Table 8 Convergence for the three-dimensional double cantilever beam with $L_x = 3$, $L_y = L_z = 1$ and $P = 1$, approximated using a regular-orthogonal mesh

N_x	N_y, N_z	N_e	N_n	Lvl	N_b	Volume V
6	2	24	63	2	962	15.2500
12	4	192	325	3	17,604	14.6806
18	6	648	931	4	112,374	14.4585
24	8	1,536	2,025	5	499,112	14.2555
30	10	3,000	3,751	6	1,474,218	14.1236
36	12	5,184	6,253	7	4,078,236	14.0543

5 Examples

The following problems were selected to showcase features and issues of the method and its implementation (named GRAND3, and provided as ESM accompanying this publication). Members with cross-sectional area $a_i < (Cutoff)_{\max}$ (a) are not plotted. Unless otherwise stated, the stress limit ratio is $\kappa = 1.0$ with $\sigma_T = 1$, the collinear tolerance is $ColTol = 0.999999$ and the plotting cutoff is $Cutoff = 0.005$.

5.1 Edge-supported (double) cantilever beam

This problem consists of a three-dimensional *box* domain, fixed at one end on two (opposite) vertical edges, and loaded at the center of the other end (Fig. 16a). The domain has dimensions $L_x = 3$ and $L_y = L_z = 1$, is loaded with $P = 1$, and is discretized with a regular partition in all three dimensions. Examples for a coarse and a fine base mesh are given in Fig. 16b and c. The optimal volumes obtained from a series of increasingly refined meshes exhibit convergence to a unique value as expected.

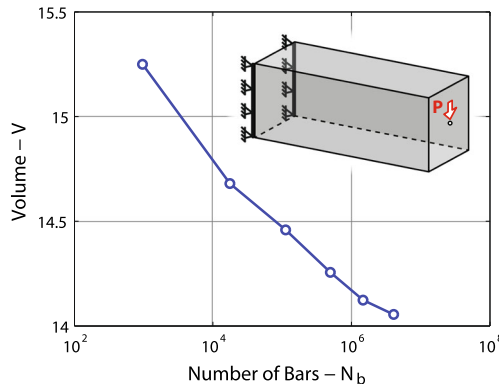


Fig. 18 Convergence of the optimal volume for the edge-supported double cantilever problem, for a set of increasingly refined ground structures

Two sample solutions obtained for the coarse and a fine base meshes are shown in Fig. 16d and e. These results hint that the optimal closed-form solution consists of two flat cantilever beams (as in Lewiński et al. (1994)), meeting at the load application point. With this assumption, a new base mesh is created for the problem: this (improved) base mesh allows for perfectly flat cantilevers to develop if the optimal structure requires it, as shown in Fig. 17a. The optimal structure obtained for this new base mesh can be seen in Fig. 17b, and confirms the flat cantilever hypothesis.

The optimal volumes obtained using regular base meshes show convergence to an absolute optimal in the vicinity of $V_{opt} \approx 13.93$: this value was obtained using the two-dimensional implementation described in Zegard and Paulino (2014). Convergence data and plots are shown in Table 8 and Fig. 18 respectively.

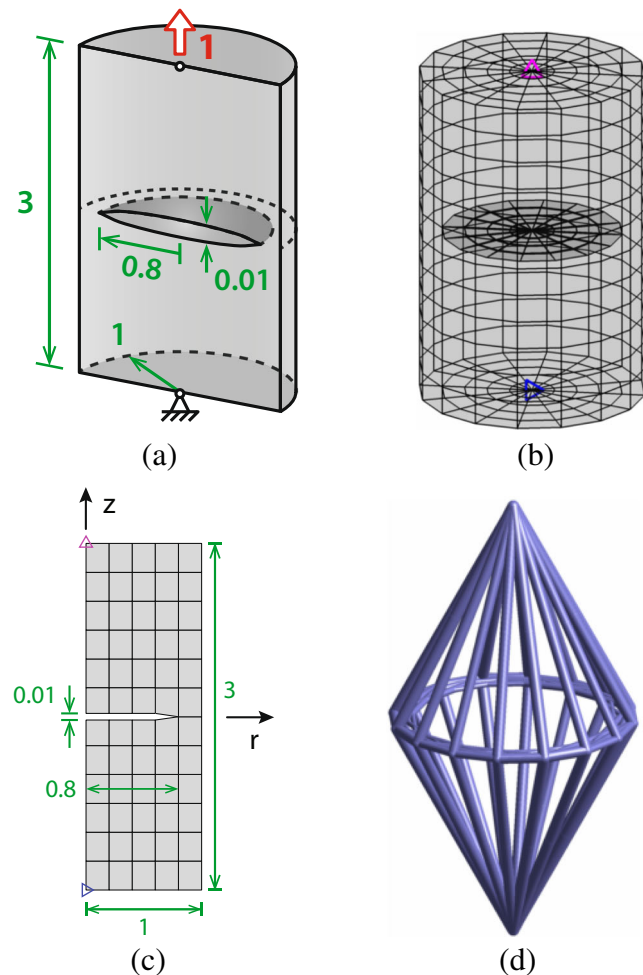


Fig. 19 Diamond problem: Vertically loaded cylinder with a coin-shaped discontinuity. **a** Half-domain with loads, boundary conditions and dimensions. **b** Base mesh used to generate the ground structure: $N_z = 12$, $N_\theta = 16$ and $N_r = 5$. **c** Axisymmetric plot of the base mesh with $N_z = 12$ and $N_r = 5$. **d** Optimal solution obtained with $Lvl = 3$ and $N_b = 109,820$

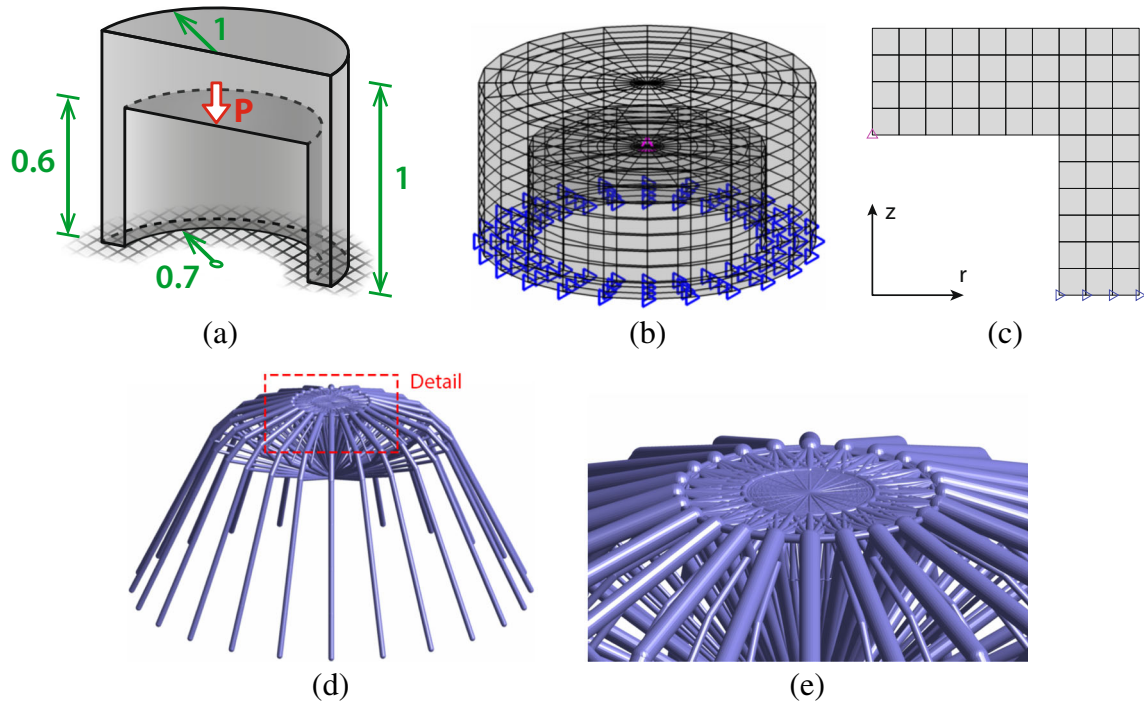


Fig. 20 Vertically loaded inverted cup problem. **a** Half-domain with loads, boundary conditions and dimensions. **b** Base mesh used to generate the ground structure. **c** Axisymmetric plot of the base mesh.

d Optimal structure generated with $Lvl = 3$ and $N_b = 168,436$, resulting in an optimal volume of $V = 2.9384$. **e** Detail of the optimal structure

5.2 Diamond problem

The diamond problem is a cylindrical domain with a coin-shaped (or disc) discontinuity in the middle. This problem shows the capability of the method to find optimal load paths for problems that include discontinuities, imperfections or barriers in their structure. The domain has a vertical load along its z axis, as shown in Fig. 19a. The domain is meshed as in Fig. 19b and c. The ground structure is generated for a $Lvl = 3$ connectivity, resulting in $N_b = 109,820$. The restriction zone is a disc primitive in the coin-shaped discontinuity. The resulting optimal structure resembles a *diamond*: the members fan away from the axis to evade the discontinuity. At the point of maximum width, it creates a *strong ring* with the purpose of shifting the member orientation back into the support as shown in Fig. 19d.

Inspecting the top part of the solution (Fig. 20e), it can be seen that this problem is degenerate; the solution lies on a facet of the feasible domain. This is not an issue of

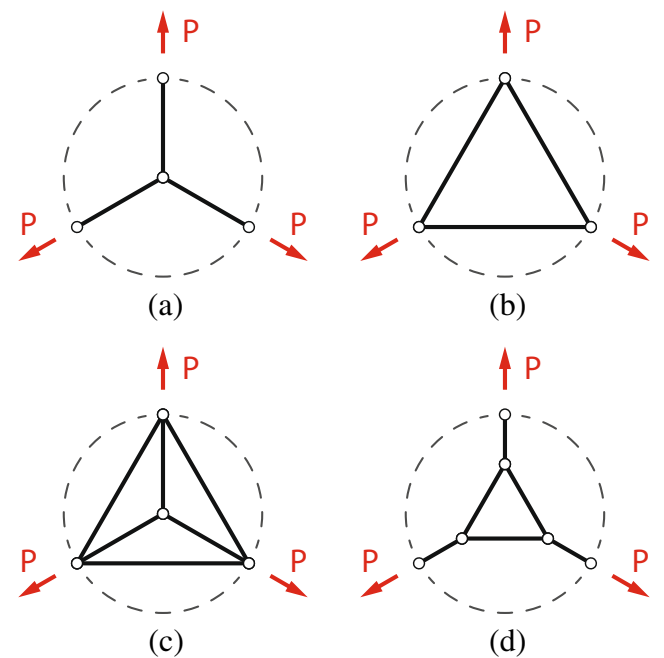


Fig. 21 Structural optimization problem with a non-unique (degenerate) solution: **a, b, c** and **d** are all optimal topologies

the ground structure method, but rather a characteristic of the problem: it does not have a unique solution (Rozvany 1997). This situation can be better understood with a simple 3 force problem (Mazurek et al. 2011): the optimal structure to carry 3 radial forces evenly distributed on a circle of radius R is not unique, as shown in Fig. 21. For the topology in Fig. 21a, the force in each member is $N_i = P$, and the length of the members is $L_i = R$. Thus, the optimal volume is:

$$V_{opt1} = 3 \left(\frac{P}{\sigma_T} \right) (R) = 3 \frac{PR}{\sigma_T}$$

Repeating the analysis for the topology in Fig. 21b, the force in each member is $N_i = P/\sqrt{3}$, and the member's length is $L_i = \sqrt{3}R$. Thus, the optimal volume is:

$$V_{opt2} = 3 \left(\frac{P/\sqrt{3}}{\sigma_T} \right) (\sqrt{3}R) = 3 \frac{PR}{\sigma_T}$$

In fact, any combination of the previous two cases, as in Fig. 21c and d for example, will result in the same optimal volume. In practice, when facing an optimal structure with a degenerate solution like in Fig. 20d, the engineer can decide the final topology. Figure 22a and b are examples of possible optimal topologies for the problem in Fig. 20e.

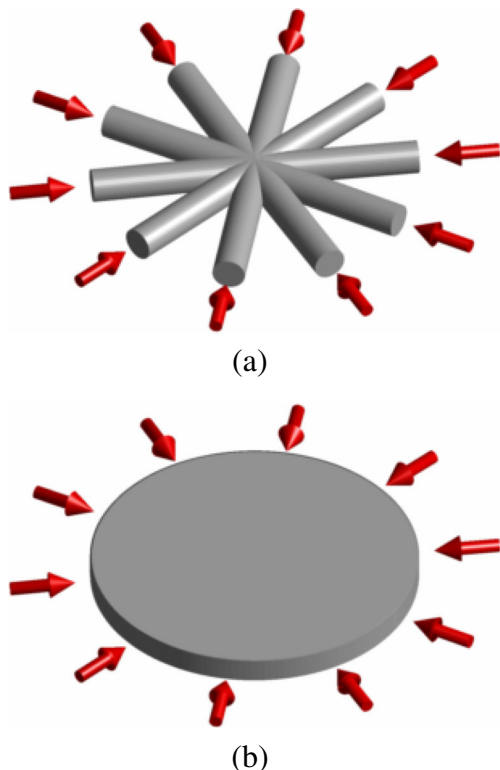


Fig. 22 Options of topologies for a degenerate problem: **a** Spoke and hub option. **b** Slab option

5.4 Crane problem

The crane (or tower) problem was introduced by Smith (1998), in whose work the domain had to be partitioned into regions in a specialized CAD system. A three-dimensional ground structure was then generated within these regions.

The approach presented here, requires no subdivision of the domain, but does require the definition of *restriction zones*. Domains are often procedurally generated using geometric primitives. Because the restriction zone is typically a subset of the primitives used to construct the domain, the additional work required is comparatively small.

The domain in Fig. 23a is discretized with two different degrees of refinement as in Fig. 23b and c. The restriction zone is the union of two *boxes* under both of the tower's

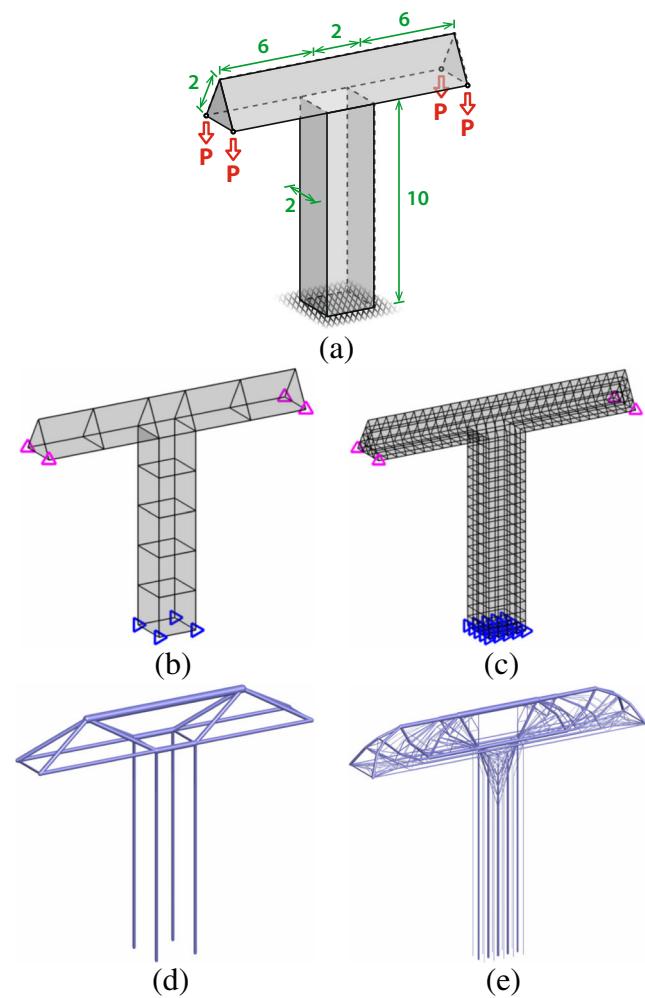
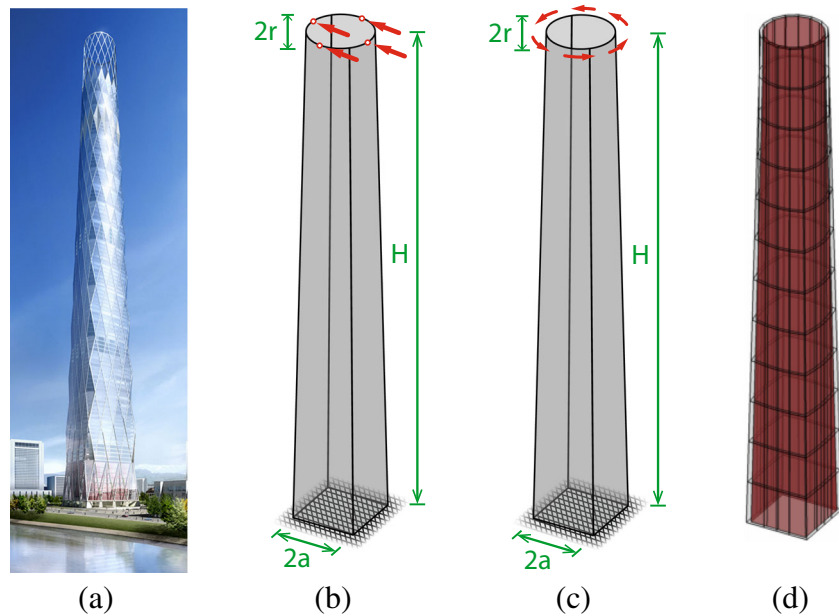


Fig. 23 Crane problem: Tower with arms loaded at four points. **a** Domain with loads, boundary conditions and dimensions. **b** Base mesh used to generate a coarse ground structure: $N_e = 10$ and $N_n = 38$. **c** Base mesh used to generate a fine ground structure: $N_e = 768$ and $N_n = 935$. **d** Solution for the coarse base mesh: $Lvl = 3$ and $N_b = 315$. **e** Solution for the fine base mesh: $Lvl = 3$ and $N_b = 47,076$; the plotting cutoff is $Cutoff = 0.002$ to prevent members from ending mid-air

Fig. 24 Lotte tower problem: **a** Rendering of the Lotte tower [© Skidmore, Owings & Merrill LLP]. **b** Domain definition, loading and boundary conditions for the laterally loaded tower. **c** Domain definition, loading and boundary conditions for the torsionally loaded tower. **d** Base mesh for the ground structure generation, with the restriction surface also shown

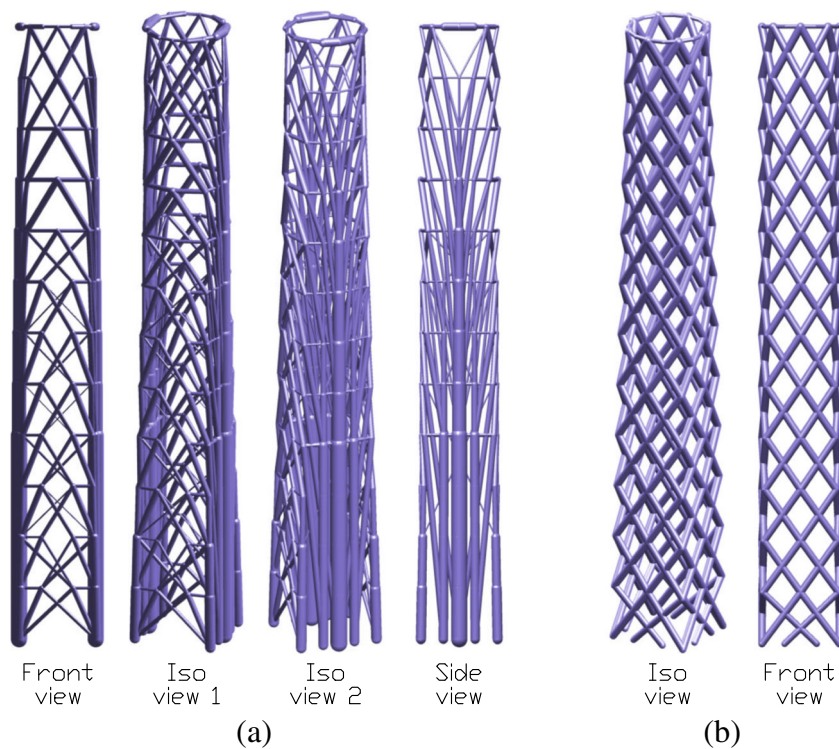


arms. The optimized ground structures for each case are shown in Fig. 23d and e. This example showcases the capability of the method (and implementation) to provide solutions with different levels of detail. Highly detailed solutions provide information into the optimal load transfer mechanism, while coarse solutions are more likely to be developed into real structures.

5.5 Lotte tower (Seoul, South Korea)

The Lotte tower is a shell-like domain (no thickness) that is square at the base and circular at the top. This problem was inspired by the design competition of the same name by Skidmore, Owings & Merrill LLP (Fig. 24a), and has been previously optimized using a density-based optimization

Fig. 25 Lotte tower problem: **a** Optimized ground structure for a lateral loading at the top. **b** Optimized ground structure for a torsional load at the top



approach by Stromberg et al. (2010). In the present example, the domain is optimized for two loading scenarios: lateral load at the tip acting at 4 points (Fig. 24b), and a torsional load distributed over the top circumference (Fig. 24c).

The domain's height is $H = 80$, the square at the base has sides $2a = 10$, and the circle at the top has a diameter of $2r = 10$. The domain is discretized using quadrangular surface elements; partitioned into $N_z = 12$ elements along its height, and $N_\theta = 16$ elements around, resulting in $N_e = 192$ and $N_n = 208$. The restriction zone is a surface primitive set-back from the interior of the domain by a small spacing, as shown in Fig. 24d.

The ground structure is generated for a $Lvl = 5$ connectivity, resulting in $N_b = 4,100$ potential members. The optimized ground structures for the lateral loading and torsional loading cases are shown in Fig. 25a and b respectively.

The lateral loading causes part of the resulting topology to work as a *web* (front view in Fig. 25a); developing an arrangement similar to an optimal cantilever, and analogous to optimal flat cantilever beams (Lewiński et al. 1994). The other side of the solution (side view in Fig. 25a) acts as a *flange*, transferring the load in tension/compression away from the *web* and to the foundation supports. On the other hand, the problem optimized for torsion results in a diagrid pattern, similar to those used in high-rise buildings.

6 Conclusions

The ground structure generation and analysis methodology presented in Zegard and Paulino (2014) is successfully extended to three-dimensional space. Concavities and holes in the domain are addressed using three-dimensional collision primitives—an extension of the two-dimensional approach. Collision primitives for a variety of shapes are developed, among which the *surface primitive* offers a viable alternative in the eventual case that no other primitive is adequate.

The method is verified and benchmarked using three problems for which the solutions are known, with the method converging to the analytical solution. Features and details of the convergence process are explored in detail. Additional problems showcase the capability of the method to address complicated domains, and to generate structures with various levels of detail. The ability to handle domains other than *boxes* has resulted in innovative bio-inspired and natural designs, as is the case with the “Diamond problem” and the “Cup domain or spider” (Figs. 19b and 20d respectively).

The rapid scaling of the complexity in three-dimensional space, make it necessary for the user to employ *engineering*

judgement in order to obtain *reasonably good* solutions for applied problems. A *good* solution is such that it can be obtained within reasonable computer time, is detailed enough, and can be manufactured. The “Lotte tower” problem loaded under torsion (Section 5.5), for example, results in a diagrid structure that is both; attractive and feasible.

Acknowledgments The authors appreciate constructive comments and insightful suggestions from the anonymous reviewers. We are thankful to the support from the US National Science Foundation under grant CMMI #1335160. We also acknowledge the support from SOM (Skidmore, Owings and Merrill LLP) and from the Donald B. and Elizabeth M. Willett endowment at the University of Illinois at Urbana–Champaign. Any opinion, finding, conclusions or recommendations expressed here are those of the authors and do not necessarily reflect the views of the sponsors.

Appendix A: – Nomenclature

A	Connectivity matrix
a	Cross-sectional areas vector
B ^T	Force equilibrium (geometric) matrix
<i>ColTol</i>	Tolerance in the collinearity check
$\hat{\mathbf{d}}$	Member's directional cosines vector
f	Nodal load vector
G	Candidate member matrix
l	Member's length vector
<i>Lvl</i>	Ground structure connectivity level
n	Internal (axial) forces vector
<i>N_b</i>	Number of bars (truss members)
<i>N_{dof}</i>	Number of degrees-of-freedom of the structure
<i>N_e</i>	Number of elements in the base mesh
<i>N_f</i>	Number of nodes with fixities
<i>N_l</i>	Number of nodes with loads
<i>N_n</i>	Number of nodes in the domain
<i>N_{sup}</i>	Number of fixed nodal components (or DOFs)
$\mathbf{s}^+, \mathbf{s}^-$	Stress constraint (positive) slack variables
<i>V</i>	Volume
κ	Tension to compression stress limit ratio
σ	Member's (axial) stresses vector
σ_T, σ_C	Stress limits in tension and compression
ϕ_F	Latitude of the the moment application ring for the torsion ball problem

Appendix B: – Collision (intersection) tests

The collision (or intersection) tests are quite common in the the video-game industry and in the field of computational geometry. While not constituting a new development, these derivations are given here for the sake of completeness. The collision primitives for the box, triangle, quadrangle and cylinder follow procedures outlined in Ericson

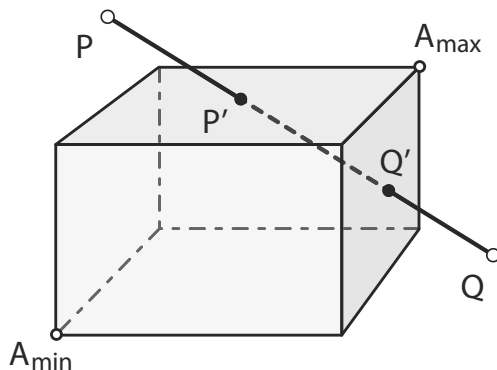


Fig. 26 Collision test between a box and a segment

(2004) with some modifications. The sphere, disc and rod⁵ were developed specifically for GRAND3, although similar procedures are likely to be found in literature given the relatively simple nature of the problem.

The surface primitive, built from the triangle and quadrangle primitives, is special; a complicated restriction volume can be translated into testing the collision on its surface. This allows the method to address complicated volumes that would be difficult to represent with the already available primitives.

B.1 Box primitive

The box primitive is defined by the coordinates of the two extreme vertices; $A_{min} = \{x_{min}, y_{min}, z_{min}\}$ and $A_{max} = \{x_{max}, y_{max}, z_{max}\}$. Given a segment \overline{PQ} , the segment's directional vector is $\mathbf{d} = \overline{PQ} = Q - P$, and any point X in the segment is defined as $X = P + t\mathbf{d}$, with $0 \leq t \leq 1$. The segment collides with the box if there is a sub-segment within \overline{PQ} contained inside the box, as shown in Fig. 26.

Defining the sub-segment $\overline{P'Q'}$, with $P' = P + t_{min}\mathbf{d}$ and $Q' = P + t_{max}\mathbf{d}$, the sub-segment is valid if $0 \leq t_{min} \leq t_{max} \leq 1$. Initially $t_{min} = 0$ and $t_{max} = 1$, positioning nodes P' and Q' at P and Q respectively. The sub-segment is then clipped by the box's 6 planes, corresponding to x_{min} , x_{max} , y_{min} , y_{max} , z_{min} and z_{max} . If the sub-segment is still valid after the clipping has been done, then the sub-segment is inside the box.

Defining a unit vector in the x direction $\hat{\mathbf{e}}_1 = \{1, 0, 0\}$, the procedure for clipping on the x plane is as follows:

$$t_1 = \frac{A_{min} \cdot \hat{\mathbf{e}}_1 - P \cdot \hat{\mathbf{e}}_1}{\mathbf{d} \cdot \hat{\mathbf{e}}_1} \quad t_2 = \frac{A_{max} \cdot \hat{\mathbf{e}}_1 - P \cdot \hat{\mathbf{e}}_1}{\mathbf{d} \cdot \hat{\mathbf{e}}_1} \quad (15)$$

Depending on the orientation of \overline{PQ} , it could occur that $t_1 > t_2$, and in such case their values are switched; $t_1 \leftarrow t_2$ and $t_2 \leftarrow t_1$. Finally, the clipping process is simply:

$$t_{min} \leftarrow \max(t_{min}, t_1) \quad t_{max} \leftarrow \min(t_{max}, t_2) \quad (16)$$

The process is then repeated for the y plane with $\hat{\mathbf{e}}_2 = \{0, 1, 0\}$, and finally the z plane with $\hat{\mathbf{e}}_3 = \{0, 0, 1\}$. The segment collides with the box if $t_{min} \leq t_{max}$ after all the clipping has been carried out. Incidentally, this procedure can address the accidental case where A_{min} and A_{max} are reversed.

B.2 Triangle primitive

Given a segment \overline{PQ} , intersecting the plane defined by points A , B and C in space at a point W (Fig. 27). The segment intersects the triangle $\triangle ABC$ if point W lies inside the triangle.

One possible solution is to find the point W , and then check if such point is inside the triangle. Assuming the triangle is defined counterclockwise: point W is inside the triangle if it is located to the left for all edges. Extending to any triangle arrangement (clockwise or counterclockwise): point W is inside the triangle if it is located to the same side for all edges. Based on this idea, the volumes of the three distinct tetrahedra can be defined by segment \overline{PQ} , and each one of the triangle's edges. These volumes can be computed by triple products, with the sign of these triple products depending on the manifold orientation of the three vectors defining the tetrahedron. If point W is found to the same side of all edges, then the sign of these volume calculations (triple products) is the same.

Defining the segment's directional vector as $\mathbf{d} = \overline{PQ} = Q - P$, then any point X within the segment is defined as $X = P + t\mathbf{d}$, with $0 \leq t \leq 1$. The normal to the triangle's plane is $\mathbf{n} = \overrightarrow{AB} \times \overrightarrow{AC}$. The intersection point with the plane of the triangle W is defined as $W = P + t_w\mathbf{d}$, with:

$$t_w = \frac{\overrightarrow{PA} \cdot \mathbf{n}}{\mathbf{d} \cdot \mathbf{n}}. \quad (17)$$

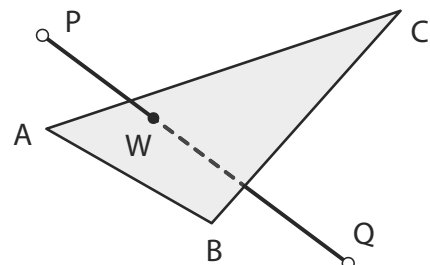


Fig. 27 Collision test between a triangle and a segment

⁵Ericson (2004) outlined a procedure for the finite cylinder. However, his derivation is flawed. The book's errata attempts to fix this, but with no success.

The triple products are defined as:

$$\begin{aligned} V_1 &= \left[\mathbf{d} \overrightarrow{PC} \overrightarrow{PB} \right] \\ V_2 &= \left[\mathbf{d} \overrightarrow{PA} \overrightarrow{PC} \right] \\ V_3 &= \left[\mathbf{d} \overrightarrow{PB} \overrightarrow{PA} \right] \end{aligned} \quad (18)$$

Finally, the segment \overrightarrow{PQ} intersects the triangle $\triangle ABC$ if and only if:

$$0 \leq t_w \leq 1 \quad \text{and} \quad \text{sign}(V_1) = \text{sign}(V_2) = \text{sign}(V_3) \quad (19)$$

B.3 Quadrangle primitive

Splitting the quadrangle into two triangles, the quadrangle is really an extension of the triangle primitive case. It is assumed that the quadrangle is flat and all 4 points lie (approximately) in the same plane. Compared to two complete triangle tests, there is a potential computational saving if one of the two triangles is chosen early in the calculations (triangles $\triangle AB_1C$ and $\triangle ACB_2$ in Fig. 28).

Defining the segment's directional vector as $\mathbf{d} = \overrightarrow{PQ} = Q - P$, then any point X within the segment is defined as $X = P + t\mathbf{d}$, with $0 \leq t \leq 1$. The normal to the quadrangle's plane is $\mathbf{n} = \overrightarrow{AB_1} \times \overrightarrow{AB_2}$. The intersection point with the plane of the quadrangle is defined as $W = P + t_w\mathbf{d}$, with:

$$t_w = \frac{\overrightarrow{PA} \cdot \mathbf{n}}{\mathbf{d} \cdot \mathbf{n}}. \quad (20)$$

The triple products are defined as:

$$\begin{aligned} V_a &= \left[\mathbf{d} \overrightarrow{PC} \overrightarrow{PB_1} \right] = \mathbf{e}_1 \cdot \overrightarrow{PB_1} \\ V_b &= \left[\mathbf{d} \overrightarrow{PC} \overrightarrow{PB_2} \right] = \mathbf{e}_1 \cdot \overrightarrow{PB_2} \\ V_2 &= - \left[\mathbf{d} \overrightarrow{PC} \overrightarrow{PA} \right] = -\mathbf{e}_1 \cdot \overrightarrow{PA}, \end{aligned} \quad (21)$$

with $\mathbf{e}_1 = \mathbf{d} \times \overrightarrow{PC}$. If the segment collides with a triangle, then all triple products must have the same sign. Thus, the

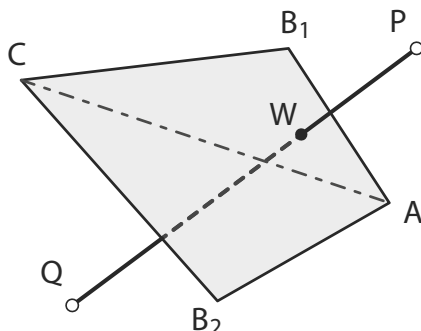


Fig. 28 Collision test between a quadrangle and a segment

correct triangle can be chosen at this stage, and the third (and last) triple product can be computed:

$$\begin{aligned} \mathbf{e}_2 &= \begin{cases} \mathbf{d} \times \overrightarrow{PB_1} & \text{if } \text{sign}(V_a) = \text{sign}(V_2) \\ \mathbf{d} \times \overrightarrow{PB_2} & \text{if } \text{sign}(V_b) = \text{sign}(V_2) \end{cases} \\ V_3 &= \mathbf{e}_2 \cdot \overrightarrow{PA} \end{aligned} \quad (22)$$

The segment collides with the quadrangle $\square AB_1CB_2$ if and only if:

$$0 \leq t_w \leq 1 \quad \text{and} \quad \text{sign}(V_2) = \text{sign}(V_3) \quad (23)$$

B.4 Sphere primitive

Defining the segment's directional vector as $\mathbf{d} = \overrightarrow{PQ} = Q - P$, then any point X in the segment is defined as $X = P + t\mathbf{d}$, with $0 \leq t \leq 1$. The segment intersects the sphere if any of the following three criteria is met (Fig. 29):

1. Point P is inside the sphere.
2. Point Q is inside the sphere.
3. The point in the segment that is closest to the sphere's center is between P and Q and inside the sphere.

Defining a vector $\mathbf{v} = C - P$, then there is collision according to the first criteria if:

$$\mathbf{v} \cdot \mathbf{v} \leq r^2 \quad (24)$$

Similarly, there is collision according to the second criteria if:

$$(\mathbf{v} - \mathbf{d}) \cdot (\mathbf{v} - \mathbf{d}) = \mathbf{v} \cdot \mathbf{v} - 2\mathbf{v} \cdot \mathbf{d} + \mathbf{d} \cdot \mathbf{d} \leq r^2 \quad (25)$$

The closest point in the line defined by P and Q to the sphere's center, measured from point P is:

$$\mathbf{w} = \frac{\mathbf{v} \cdot \mathbf{d}}{\mathbf{d} \cdot \mathbf{d}} \mathbf{d} \quad (26)$$

This point is inside the sphere if:

$$\begin{aligned} (\mathbf{v} - \mathbf{w}) \cdot (\mathbf{v} - \mathbf{w}) &\leq r^2 \\ \left(\mathbf{v} - \frac{\mathbf{v} \cdot \mathbf{d}}{\mathbf{d} \cdot \mathbf{d}} \mathbf{d} \right) \cdot \left(\mathbf{v} - \frac{\mathbf{v} \cdot \mathbf{d}}{\mathbf{d} \cdot \mathbf{d}} \mathbf{d} \right) &\leq r^2, \end{aligned} \quad (27)$$

with this point inside the segment \overrightarrow{PQ} if and only if $0 \leq \mathbf{w} \cdot \mathbf{d} \leq \mathbf{d} \cdot \mathbf{d}$, which is an equivalent expression to $0 \leq t \leq 1$.

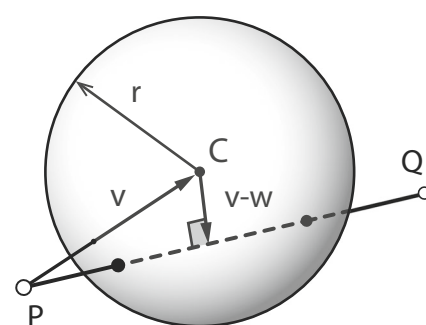


Fig. 29 Collision test between a sphere and a segment

B.5 Disc primitive

Defining the segment's directional vector as $\mathbf{d} = \overrightarrow{PQ} = Q - P$, then any point X in the segment is defined as $X = P + t\mathbf{d}$, with $0 \leq t \leq 1$.

The disc is centered at point A , and the normal points towards a point B as in Fig. 30. The normal to the plane of the disc is $\mathbf{n} = B - A$. Defining $\mathbf{v} = \overrightarrow{AP} = P - A$, the intersection with the disc's plane is found at a point $W = P + t_w\mathbf{d}$:

$$t_w = -\frac{\mathbf{v} \cdot \mathbf{n}}{\mathbf{d} \cdot \mathbf{n}} \quad (28)$$

The segment collides with the disc if the distance between point W and the disc's center A is less than or equal to the disc's radius:

$$\overrightarrow{AW} = W - A = P - A + t_w\mathbf{d} = \mathbf{v} - \frac{\mathbf{v} \cdot \mathbf{n}}{\mathbf{d} \cdot \mathbf{n}}\mathbf{d} \quad (29)$$

Finally, the segment collides with the disc if and only if:

$$\overrightarrow{AW} \cdot \overrightarrow{AW} = \left(\mathbf{v} - \frac{\mathbf{v} \cdot \mathbf{n}}{\mathbf{d} \cdot \mathbf{n}}\mathbf{d} \right) \cdot \left(\mathbf{v} - \frac{\mathbf{v} \cdot \mathbf{n}}{\mathbf{d} \cdot \mathbf{n}}\mathbf{d} \right) \leq r^2, \quad (30)$$

with $0 \leq t_w \leq 1$.

B.6 Cylinder primitive (infinite cylinder)

Defining the segment's directional vector as $\mathbf{d} = \overrightarrow{PQ} = Q - P$, then any point X in the segment is defined as $X = P + t\mathbf{d}$, with $0 \leq t \leq 1$. The segment is found to collide with the (infinite) cylinder if:

1. The segment collides with the cylinder's surface.
2. The segment is completely contained within the cylinder.

The cylinder's axis is defined by $\mathbf{n} = B - A$ as in Fig. 31. The intersection with the cylinder's surface is found at points $W = P + t_w\mathbf{d}$. Defining the radial vector of length r from the cylinder's axis to point W as \mathbf{m} , then:

$$0 = \mathbf{m} \cdot \mathbf{m} - r^2$$

$$0 = \left(\overrightarrow{AW} - \frac{\overrightarrow{AW} \cdot \mathbf{n}}{\mathbf{n} \cdot \mathbf{n}}\mathbf{n} \right) \cdot \left(\overrightarrow{AW} - \frac{\overrightarrow{AW} \cdot \mathbf{n}}{\mathbf{n} \cdot \mathbf{n}}\mathbf{n} \right) - r^2 \quad (31)$$

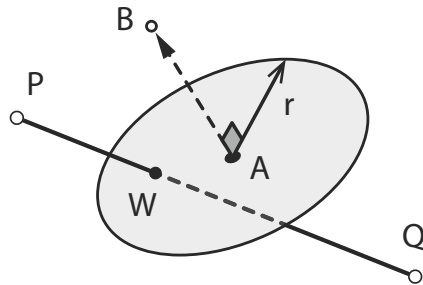


Fig. 30 Collision test between a disc and a segment

Defining $\mathbf{v} = \overrightarrow{AP} = P - A$, and expanding \overrightarrow{AW} in terms of \mathbf{v} , \mathbf{d} and t_w :

$$0 = \left((\mathbf{v} + t_w\mathbf{d}) - \left[\frac{(\mathbf{v} + t_w\mathbf{d}) \cdot \mathbf{n}}{\mathbf{n} \cdot \mathbf{n}} \right] \mathbf{n} \right) \cdot \left((\mathbf{v} + t_w\mathbf{d}) - \left[\frac{(\mathbf{v} + t_w\mathbf{d}) \cdot \mathbf{n}}{\mathbf{n} \cdot \mathbf{n}} \right] \mathbf{n} \right) - r^2, \quad (32)$$

where terms can be ordered to obtain a quadratic equation for t_w :

$$0 = \left[\mathbf{d} \cdot \mathbf{d} - \frac{(\mathbf{d} \cdot \mathbf{n})^2}{\mathbf{n} \cdot \mathbf{n}} \right] t_w^2 + 2 \left[\mathbf{v} \cdot \mathbf{d} - \frac{(\mathbf{d} \cdot \mathbf{n})(\mathbf{v} \cdot \mathbf{n})}{\mathbf{n} \cdot \mathbf{n}} \right] t_w + (\mathbf{v} \cdot \mathbf{v}) - \frac{(\mathbf{v} \cdot \mathbf{n})^2}{\mathbf{n} \cdot \mathbf{n}} - r^2 \quad (33)$$

Multiplying by $\mathbf{n} \cdot \mathbf{n}$, the quadratic equation becomes:

$$0 = at_w^2 + bt_w + c$$

$$a = (\mathbf{n} \cdot \mathbf{n})(\mathbf{d} \cdot \mathbf{d}) - (\mathbf{d} \cdot \mathbf{n})^2$$

$$\frac{b}{2} = (\mathbf{n} \cdot \mathbf{n})(\mathbf{v} \cdot \mathbf{d}) - (\mathbf{d} \cdot \mathbf{n})(\mathbf{v} \cdot \mathbf{n})$$

$$c = (\mathbf{n} \cdot \mathbf{n}) \left[(\mathbf{v} \cdot \mathbf{v}) - r^2 \right] - (\mathbf{v} \cdot \mathbf{n})^2, \quad (34)$$

with solutions given by:

$$t_w = \frac{-b \pm \sqrt{b^2 - 4ac}}{2a} = \frac{-\frac{b}{2} \pm \sqrt{\left(\frac{b}{2}\right)^2 - ac}}{a} \quad (35)$$

The (infinite) line defined by the segment does not intersect the cylinder if the discriminant in (35) is negative (i.e. $(b/2)^2 - ac < 0$). If the discriminant is positive, then an additional check must be made to ensure the intersection point is within the segment PQ . The segment collides with the cylinder if $0 \leq t_w \leq 1$ for any of the two roots (points W and W' in Fig. 31).

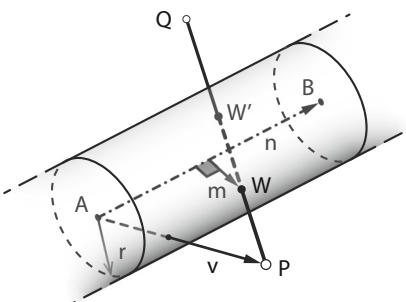


Fig. 31 Collision test between a cylinder (infinite length) and a segment

Finally, the segment is completely contained inside the cylinder, if the distance from the cylinder's axis to point P is less than or equal to the radius r :

$$\left(\mathbf{v} - \frac{\mathbf{v} \cdot \mathbf{n}}{\mathbf{n} \cdot \mathbf{n}} \mathbf{n}\right) \cdot \left(\mathbf{v} - \frac{\mathbf{v} \cdot \mathbf{n}}{\mathbf{n} \cdot \mathbf{n}} \mathbf{n}\right) \leq r^2 \quad (36)$$

B.7 Rod primitive

The rod primitive is a combination of the infinite cylinder and disc primitives with some minor modifications. The segment collides with the rod if any of the following 4 situations occur:

- The segment collides with the finite cylinder's surface.
- The segment collides with the A endcap (disc).
- The segment collides with the B endcap (disc).
- The segment is fully contained within the rod.

The collision with the finite cylinder's surface begins from the test primitive for the infinite cylinder outlined in (34) and (35). In addition, the intersection points W and W' (Fig. 32) must be in the surface between the endcaps. Thus, an additional check is required; the segment collides with the finite cylinder's surface if:

$$\begin{aligned} 0 \leq \mathbf{w} \cdot \mathbf{n} \leq \mathbf{n} \cdot \mathbf{n} \\ 0 \leq (\mathbf{v} + t_w \mathbf{d}) \cdot \mathbf{n} \leq \mathbf{n} \cdot \mathbf{n} \end{aligned} \quad (37)$$

for any of the two roots of t_w from (35), with $0 \leq t_w \leq 1$.

The collision with the endcaps A and B follow the procedure for the disc primitive. Equation (30) can be used with no modification to test the collision against endcap A . The

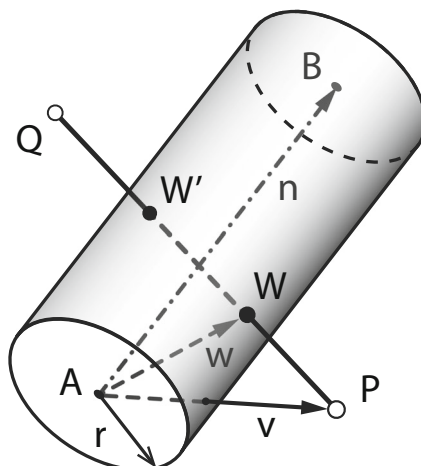


Fig. 32 Collision test between a rod (finite cylinder with endcaps) and a segment

B endcap is analogous to the endcap A ; the segment collides with endcap B if:

$$\begin{aligned} \overrightarrow{BW} \cdot \overrightarrow{BW} \leq r^2 \\ \left(\mathbf{v} + \frac{\mathbf{n} \cdot \mathbf{n} - \mathbf{v} \cdot \mathbf{n}}{\mathbf{d} \cdot \mathbf{n}} \mathbf{d}\right) \cdot \left(\mathbf{v} + \frac{\mathbf{n} \cdot \mathbf{n} - \mathbf{v} \cdot \mathbf{n}}{\mathbf{d} \cdot \mathbf{n}} \mathbf{d}\right) \leq r^2, \end{aligned} \quad (38)$$

with:

$$0 \leq \left(t_w = \frac{\mathbf{n} \cdot \mathbf{n} - \mathbf{v} \cdot \mathbf{n}}{\mathbf{d} \cdot \mathbf{n}}\right) \leq 1 \quad (39)$$

Finally, if the segment is completely contained in the rod, then point P must be inside the rod. In other words, if the distance from point P to the cylinder's axis is less than or equal to r :

$$\left(\mathbf{v} - \frac{\mathbf{v} \cdot \mathbf{n}}{\mathbf{n} \cdot \mathbf{n}} \mathbf{n}\right) \cdot \left(\mathbf{v} - \frac{\mathbf{v} \cdot \mathbf{n}}{\mathbf{n} \cdot \mathbf{n}} \mathbf{n}\right) \leq r^2, \quad (40)$$

with an additional check to verify point A is between the endcaps:

$$0 \leq \frac{\mathbf{v} \cdot \mathbf{n}}{\mathbf{n} \cdot \mathbf{n}} \leq 1 \quad (41)$$

B.8 Surface primitive

The surface primitive builds from the base of the triangle and quadrangle primitives. The surface primitive can handle any surface provided that it is tessellated (discretized) and the points in each facet lie (approximately) in the same plane. In addition, it is assumed that all facets are convex in their own plane. An example of a tessellated surface is shown in Fig. 33: the surface was tessellated using triangles and quadrangles. The inputs for this collision primitive are:

- A matrix of nodes RNODE of size $N_{rn} \times 3$, where N_{rn} is the number of nodes in the collision surface.
- A list (cell) with facet connectivity RFACE of size $N_{rf} \times 1$, where N_{rf} is the number of facets in the collision surface. Each entry in RFACE is a row vector with nodal connectivity (based on RNODE).

The surface collision primitive can address facets with more than 4 nodes (flat polygons), provided that all the nodes lie in (approximately) the same plane. This polygon will be subdivided into triangles and evaluated sequentially.

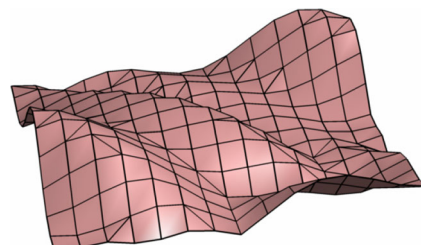
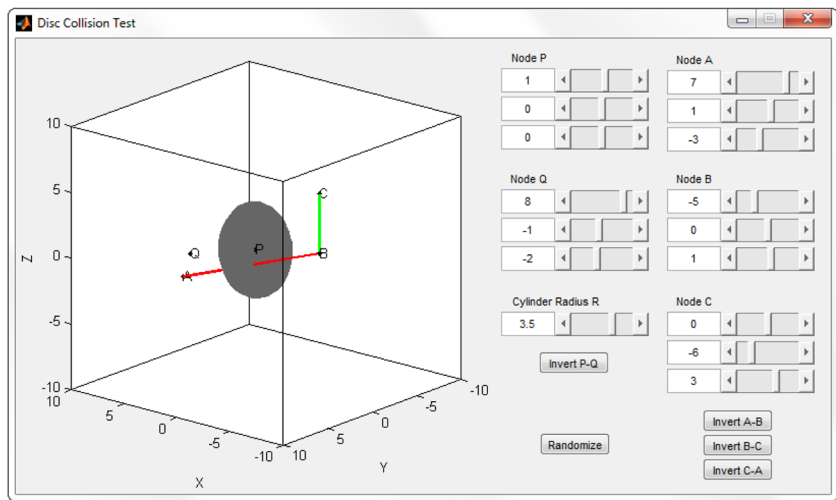


Fig. 33 Collision surface example: Surface is tessellated into triangles and quadrangles

Fig. 34 User interface for live testing and debugging the disc collision primitive



B.9 Development & debugging of collision tests

Algorithms for additional intersection tests can be found in literature or derived. It is strongly recommended however, to test and debug new collision primitives thoroughly. In the present work for example, simple game-like user interfaces were used for live testing the collision primitives (see Fig. 34 for an example).

References

- Achtziger W (2007) On simultaneous optimization of truss geometry and topology. *Struct Multidiscip Optim* 33(4–5):285–304
- Barber CB, Dobkin DP, Huhdanpaa H (1996) The quickhull algorithm for convex hulls. *ACM Trans Math Softw* 22(4):469–483. <http://www.qhull.org/>
- Christensen P, Klarbring A (2009) An introduction to structural optimization, 1st edn. Springer, Berlin
- Dorn WS, Gomory RE, Greenberg HJ (1964) Automatic design of optimal structures. *J Mech* 3(1):25–52
- Ericson C (2004) Real-time collision detection, 1st edn. Morgan Kaufmann, San Francisco
- Gerdes D (1994) Strukturoptimierung unter Anwendung der Optimitätskriterien auf diskretisierte Tragwerke bei besonderer Berücksichtigung der Stabilität (in German). Phd thesis, Universität Essen
- Gilbert M, Darwiche W, Tyas A, Shepherd P (2005) Application of large-scale layout optimization techniques in structural engineering practice. In: 6th world congress of structural and multidisciplinary optimization, June:1–10
- Gilbert M, Tyas A (2003) Layout optimization of large-scale pin-jointed frames. *Eng Comput* 20(8):1044–1064
- Hemp WS (1973) Optimum structures, 1st edn. Oxford University Press, Oxford
- Hencky H (1923) Über einige statisch bestimmte Fälle des Gleichgewichts in plastischen Körpern. *Z Angew Math Mech* 747:241–251
- Herceg M, Kvasnica M, Jones CN, Morari M (2013) Multi-parametric toolbox 3.0. In: Proceedings of the European control conference, Zürich, pp 502–510. <http://control.ee.ethz.ch/~mpt>
- Karmarkar N (1984) A new polynomial-time algorithm for linear programming. *Combinatorica* 4(4):373–395
- Kicher TP (1966) Optimum design-minimum weight versus fully stressed. *ASCE Journal of Structural Division* 92(ST 6):265–279
- Kirsch U (1993) Structural optimization: fundamentals and applications, 1st edn. Springer, Berlin
- Lewiński T (2004) Michell structures formed on surfaces of revolution. *Struct Multidiscip Optim* 28(1):20–30
- Lewiński T, Zhou M, Rozvany GIN (1994) Extended exact solutions for least-weight truss layouts—Part I: cantilever with a horizontal axis of symmetry. *Int J Mech Sci* 36(5):375–398
- Mazurek A, Baker WF, Tort C (2011) Geometrical aspects of optimum truss like structures. *Struct Multidiscip Optim* 43(2):231–242
- Michell AGM (1904) The limits of economy of material in frame-structures. *Philosophical Magazine Series* 6 8(47):589–597
- Ohsaki M (2010) Optimization of finite dimensional structures, 1st edn. CRC Press, Boca Raton
- Rozvany GIN (1997) On the validity of Prager's example of nonunique Michell structures. *Structural Optimization* 13(2–3):191–194
- Rycroft CH (2014) Voro++ v0.4.6: a three-dimensional Voronoi cell library in C++. <http://math.lbl.gov/voro++/>. Accessed 21 April 2014
- Smith ODS (1998) Generation of ground structures for 2D and 3D design domains. *Eng Comput* 15(4):462–500
- Sokół T (2011) A 99 line code for discretized Michell truss optimization written in mathematica. *Struct Multidiscip Optim* 43(2):181–190
- Stromberg LL, Beghini A, Baker WF, Paulino GH (2010) Application of layout and topology optimization using pattern gradation for the conceptual design of buildings. *Struct Multidiscip Optim* 43(2):165–180
- Sved G (1954) The minimum weight of certain redundant structures. *Austral J Appl Sci* 5:1–9
- Tyas A, Gilbert M, Pritchard T (2006) Practical plastic layout optimization of trusses incorporating stability considerations. *Comput Struct* 84(3–4):115–126
- Wright MH (2004) The interior-point revolution in optimization: history, recent developments, and lasting consequences. *Bull Am Math Soc* 42(1):39–56
- Zegard T, Paulino GH (2014) GRAND – Ground structure based topology optimization on arbitrary 2D domains using MATLAB. *Struct Multidiscip Optim* 50(5):861–882